

Possible Organization for Writing a Thesis including a L^AT_EXFramework and
Examples

by

A Graduate Advisor
B.Sc., University of WhoKnowsWhere, 2053
M.Sc., University of AnotherOne, 2054

A Dissertation Submitted in Partial Fulfillment of the
Requirements for the Degree of

DOCTOR OF PHILOSOPHY

in the Department of Whichever

© Graduate Advisor, 2008
University of Victoria

All rights reserved. This dissertation may not be reproduced in whole or in part, by
photocopying or other means, without the permission of the author.

Possible Organization for Writing a Thesis including a L^AT_EXFramework and
Examples

by

A Graduate Advisor
B.Sc., University of WhoKnowsWhere, 2053
M.Sc., University of AnotherOne, 2054

Supervisory Committee

Dr. R. Supervisor Main, Supervisor
(Department of Same As Candidate)

Dr. M. Member One, Departmental Member
(Department of Same As Candidate)

Dr. Member Two, Departmental Member
(Department of Same As Candidate)

Dr. Outside Member, Outside Member
(Department of Not Same As Candidate)

Supervisory Committee

Dr. R. Supervisor Main, Supervisor
(Department of Same As Candidate)

Dr. M. Member One, Departmental Member
(Department of Same As Candidate)

Dr. Member Two, Departmental Member
(Department of Same As Candidate)

Dr. Outside Member, Outside Member
(Department of Not Same As Candidate)

ABSTRACT

This document is a possible Latex framework for a thesis or dissertation at UVic. It should work in the Windows, Mac and Unix environments. The content is based on the experience of one supervisor and graduate advisor. It explains the organization that can help write a thesis, especially in a scientific environment where the research contains experimental results as well. There is no claim that this is the *best* or *only* way to structure such a document. Yet in the majority of cases it serves extremely well as a sound basis which can be customized according to the requirements of the members of the supervisory committee and the topic of research. Additionally some examples on using L^AT_EXare included as a bonus for beginners.

Contents

Supervisory Committee	ii
Abstract	iii
Table of Contents	iv
List of Tables	vi
List of Figures	vii
Acknowledgements	ix
Dedication	x
1 Introduction	1
2 Theory	2
2.1 The Standard Model	2
2.1.1 The Particles	2
2.1.2 Quantum Electrodynamics (QED)	4
2.1.3 Weak Interactions	4
2.1.4 Quantum Chromodynamics (QCD)	5
2.1.5 The Higgs Boson	6
2.2 Beyond the Standard Model	7
2.2.1 Dark Matter	8
2.2.2 Dark Higgs Boson Model	9
3 The Large Hadron Collider and the ATLAS Experiment	11
3.1 The Large Hadron Collider	11
3.2 The ATLAS Experiment	13

3.2.1	Inner Tracking Detector	15
3.2.2	Calorimeters	16
3.2.3	Muon Spectrometers	18
3.2.4	Trigger and Data Acquisition	19
4	Analysis Preparation	20
4.1	Signal Model	20
4.2	Monte Carlo Production and Data	22
4.2.1	Signal MC	22
4.2.2	Background MC	23
4.2.3	Data	24
4.3	Object Definition	25
4.3.1	Muons	25
4.3.2	Electrons	26
4.3.3	Small-radius ($R = 0.4$) Jets	27
4.3.4	Track-Assisted-Reclustered Jets	28
4.3.5	Missing Transverse Momentum (E_T^{miss})	29
5	Analysis	31
5.1	Cut and Count Analysis	31
5.2	Analysis Strategy	32
5.3	Merged Signal Region	32
5.3.1	Signal and Background Characterization	33
5.3.2	TAR Jet Lepton Disentanglement	33
5.3.3	Merged Signal Region Optimization	35
5.4	Resolved Signal Region	40
5.5	$t\bar{t}$ Control Regions	40
5.6	$W+jets$ Control Region	42
6	Conclusions	48
A	Additional Information	49
A.1	Preselection level plots	49
Bibliography		53

List of Tables

Table 4.1 Muon object definition criteria	26
Table 4.2 Electron object definition criteria	27
Table 4.3 $R = 0.4$ jets object definition criteria	27
Table 4.4 TAR jet reconstruction parameters	29
Table 5.1 Optimized selection criteria for the “merged” category signal region.	39

List of Figures

Figure 2.1 The elementary particles of the Standard Model	3
Figure 2.2 The fundamental QED vertex.	4
Figure 2.3 Some fundamental weak interaction vertices.	5
Figure 2.4 Some fundamental QCD interaction vertices.	6
Figure 2.5 Shapes of the Higgs Potential for different cases of μ^2	7
Figure 2.6 The bullet cluster showing separation of x-ray density (pink) and gravitational density (blue).	9
Figure 3.1 Overview of the CERN accelerator complex, including the LHC injector system and surrounding experiments.	12
Figure 3.2 A cut-out overview of the ATLAS detector and main components. Diagram from [5].	14
Figure 3.3 A cut-out view of the ATLAS inner detector. Diagram from [5].	15
Figure 3.4 A cut-out view of the ATLAS calorimeter system. Diagram from [5].	16
Figure 3.5 A cut-out view of the ATLAS muon spectrometer system. Diagram from [5].	18
Figure 4.1 Branching fractions for a SM Higgs boson as a fraction of the Higgs boson mass [19].	21
Figure 4.2 DH Decay	21
Figure 4.3 Signal point locations in m_s vs. $m_{Z'}$ parameter space. Blue points represent the original signal grid while green points are added in the second signal grid	23
Figure 4.4 A visual summary of the TAR Jet algorithm.	29
Figure 5.1 Schematic representation of the differing reconstruction technique between merged and resolved regions.	32

Figure 5.2 Normalized $R = 1.0$ TAR jet mass distributions with and without lepton disentanglement applied for several representative signal points	35
Figure 5.3 TAR jet mass distributions for two representative signal points compared with constituent anti- k_t $R = 0.4$ vs. anti- k_t $R = 0.2$ jets. Left: sample signal point at $(m_s, m_{Z'}) = (310, 500)$ GeV. Right: sample signal point at $(m_s, m_{Z'}) = (160, 1700)$ GeV	36
Figure 5.4 N-1 plots in the “merged” signal region.	41
Figure 5.5 $t\bar{t}$ yield in the “merged” $t\bar{t}$ control region for various E_T^{miss} significance cut placements	42
Figure 5.6 Data-MC Comparisons in the “merged” $t\bar{t}$ control region	43
Figure 5.7 Data-MC Comparisons in the “resolved” $t\bar{t}$ control region	44
Figure 5.8 Data-MC comparisons in the “merged” $W + \text{jets}$ control region	46
Figure 5.9 Data-MC comparisons in the “resolved” $W + \text{jets}$ control region	47
Figure A.1 N-1 plots in the “merged” signal region.	50
Figure A.2 N-1 plots in the “merged” signal region.	51
Figure A.3 N-1 plots in the “merged” signal region.	52

ACKNOWLEDGEMENTS

I would like to thank:

my cat, Star Trek, and the weather, for supporting me in the low moments.

Supervisor Main, for mentoring, support, encouragement, and patience.

Grant Organization Name, for funding me with a Scholarship.

I believe I know the only cure, which is to make one's centre of life inside of one's self, not selfishly or exclusively, but with a kind of unassailable serenity-to decorate one's inner house so richly that one is content there, glad to welcome any one who wants to come and stay, but happy all the same in the hours when one is inevitably alone.

Edith Wharton

DEDICATION

Just hoping this is useful!

Chapter 1

Introduction

Chapter 2

Theory

The **Standard Model of Particle Physics (SM)** [36, 39, 28, 27] is a quantized relativistic field theory that describes all known elementary particles, as well as their interactions via three of the four known fundamental forces. It has been tested extremely rigorously since its development in the 1960s and 1970s, and in every case its predictions have held true. The final piece of the puzzle fell into place with the experimental verification of the existence of the Higgs Boson in 2012 [4].

Despite its success, however, the SM is considered an incomplete theory. It does not describe the interaction of matter via the fourth fundamental force, gravity, nor does it account for the existence of *dark matter* in our universe, or the asymmetry between the observed amounts matter and anti-matter. These shortcomings provide motivation to extend the SM by searching beyond it for new phenomena.

This chapter will provide a short overview of the SM theory, before describing some of the deficiencies that motivate an extension of it.

2.1 The Standard Model

2.1.1 The Particles

The elementary particles of the Standard Model are shown in Figure 2.1. They can be categorized into two groups: *fermions* and *bosons*. *Fermions* carry half-integer spin, and constitute the matter that surrounds us. For each fermion there also exists a corresponding anti-particle with an opposite electric charge. In this document anti-particles will be denoted either by the charge (e.g. e^+ vs. e^-) or by a bar overhead e.g. (t vs. \bar{t}). The fermions can be further divided into two groups: *leptons* and

quarks. *Leptons*, the most familiar of which is the electron, interact via the weak force and, if electrically charged, the electromagnetic force. They come in three flavour generations, each of which has a neutral particle (*neutrino*) and a charged fermion with electric charge -1. Unlike leptons, which regularly exist freely, *quarks* exist mostly in bound states called *hadrons*, the most well-known of which are the proton and neutron composed of (u, u, d) and (u, d, d) quarks respectively. Like leptons, quarks come in three generations, each of which has a pair of particles with electric charges $+2/3$ and $-1/3$. They interact via all three forces of the standard model: strong, weak, and electromagnetic.

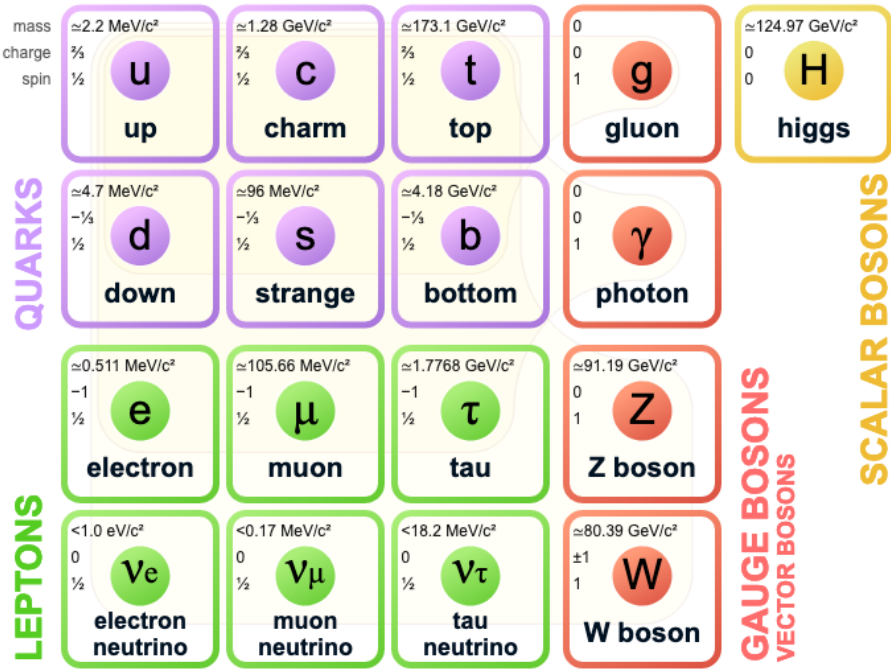


Figure 2.1: The elementary particles of the Standard Model

Bosons carry integer spin, and mediate the forces via which particles interact. Massless *gluons* and *photons* as well as massive W and Z bosons are spin-1 vector bosons, while the Higgs Boson is a spin-0 scalar boson. The massive W and Z vector bosons are the carriers of the weak force, the photon carries the electromagnetic force, and the gluons carry the strong force binding quarks. Along with interacting with fermions via exchange, bosons are also able to interact among themselves. W bosons are able to directly interact with both Z bosons and photons, as well as self-interacting. Gluons can also self-interact, but Z bosons and photons cannot. The Higgs boson interacts with all massive particles, including self-interaction, and it is

via their interaction with the Higgs field that massive bosons obtain their mass.

2.1.2 Quantum Electrodynamics (QED)

Quantum Electrodynamics (QED) [23, 39, 36] is a quantum field theory of electrodynamics and the electromagnetic force. It describes the interaction of electrically charged particles via the exchange of photons. Mathematically, QED is an abelian (commutative) gauge theory with the gauge group $U(1)$. The fundamental interactions of the theory are: the emission or absorption of a single photon by a charged particle and the creation or annihilation of a pair of charged particles. These interactions can each be represented by various orientations of the Feynman vertex shown in Figure 2.2.

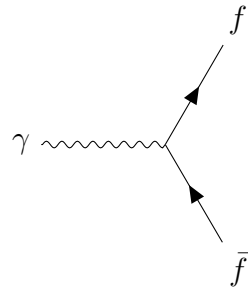


Figure 2.2: The fundamental QED vertex.

2.1.3 Weak Interactions

The weak force [28, 25, 26, 43], in contrast to the electromagnetic force, is mediated by the exchange of massive vector bosons W^+ , W^- , and Z . Owing to the charge of the W bosons, and the fact in contrast to the electromagnetic force neutral fermions also interact via the weak force, there are many more possible fundamental interactions. Figure 2.3 shows the vertices corresponding three such interactions: fermions interacting with the Z boson in a similar vertex to that of Figure 2.2 shown in (a), a charged lepton and neutrino interacting with a W boson shown in (b), and a quark-antiquark pair interacting with a W boson shown in (c).

At high energy scales, the aforementioned electromagnetic force and the weak force unify to become the electroweak interaction. Glashow, Salam, and Weinberg's Electroweak theory unites the two forces into a single $U(1) \otimes SU(2)$ gauge theory.

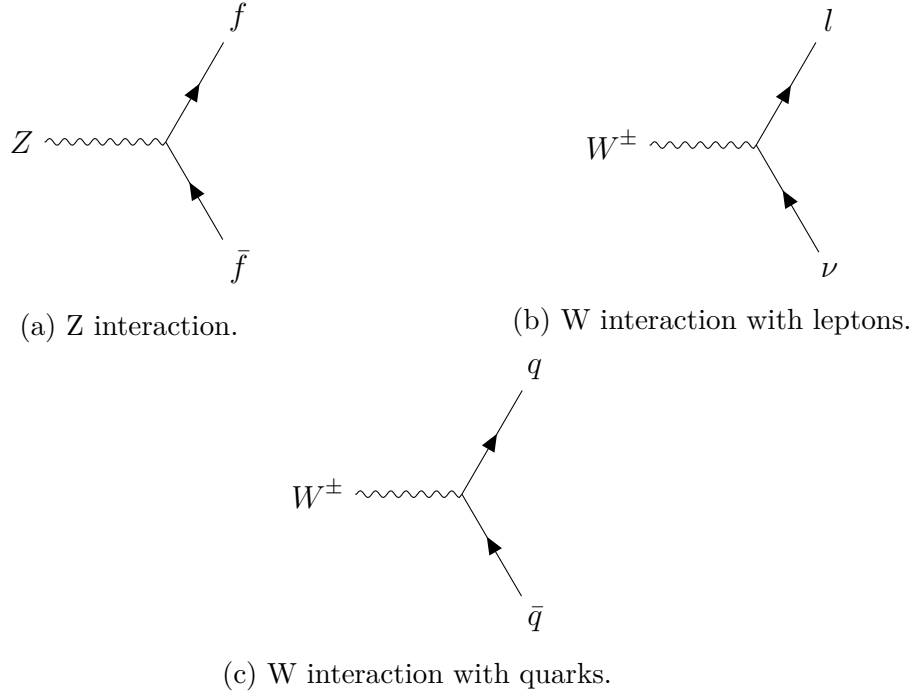


Figure 2.3: Some fundamental weak interaction vertices.

2.1.4 Quantum Chromodynamics (QCD)

Quantum Chromodynamics (QCD) [28, 16] is the theory describing the strong interaction between gluons and quarks. It is again a gauge theory, this time with the SU(3) symmetry group. There are three colour charges associated with this group, which are carried by both quarks and gluons. Each of the 8 gluons carries a unique colour charge and anti colour charge pair, while quarks carry a single colour charge. Because they carry colour charge, gluons are able to both interact with quarks and self-interact. This gives rise to several possible interaction vertices in the theory, some of which are shown in Figure 2.4.

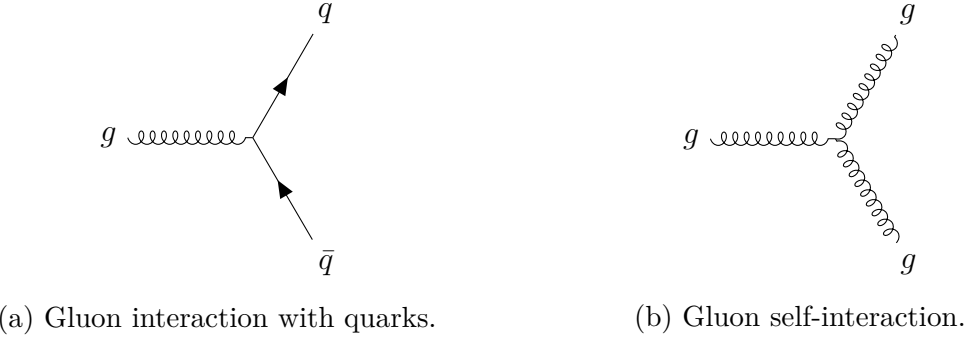


Figure 2.4: Some fundamental QCD interaction vertices.

2.1.5 The Higgs Boson

Electroweak theory alone does not contain a mechanism to provide particles with mass. This contrasts with the observed reality that all fermions as well as W and Z bosons are in fact massive. If the lagrangian of these theories were to contain mass terms, they would lose their gauge invariance and the standard model would not be renormalizable. Instead, these particles acquire their mass through the *Higgs Mechanism* [21, 29, 30].

THIS PLOT BELOW IS FOR THE U(1) HIGGS - SIMPLIFICATION

A new Higgs Field Φ is introduced, with a Lagrangian which can be written as:

$$\mathcal{L}_{Higgs} = (D_\mu \Phi)^\dagger D^\mu \Phi + V(\Phi) \quad (2.1)$$

Where D_μ is the gauge covariant derivative of the electroweak theory. In order for the Lagrangian to remain gauge invariant the Higgs potential $V(\Phi)$ must take the form:

$$V(\Phi) = \mu^2 \Phi + \lambda \Phi^4 \quad (2.2)$$

where λ and Φ are free parameters. λ is forced to be greater than 0 by requiring that the potential have a stable minimum. This leads the potential to have two different possible shapes, shown in Figure 2.5, given the sign of μ^2 :

1. $\mu^2 > 0$: The trivial case of a parabolic potential with a minimum at $\Phi = 0$ arises.

2. $\mu^2 > 0$: A potential with a minimum at:

$$|\Phi| = v = \sqrt{\frac{\mu^2}{\lambda}} \quad (2.3)$$

arises, where v is known as the vacuum expectation value. This minimum is occupied by infinitely degenerate states. This is the case that gives rise to the Higgs mechanism.

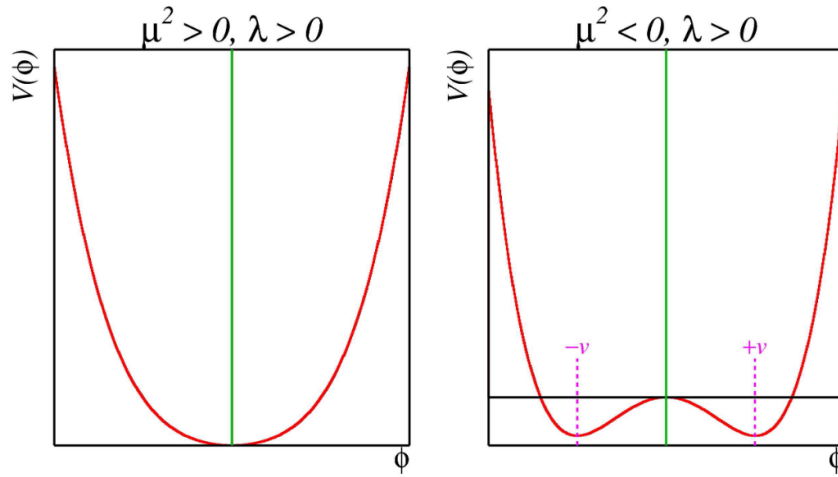


Figure 2.5: Shapes of the Higgs Potential for different cases of μ^2 .

In the second case, the ground states occupying the minimum are not equivalent under gauge transformation, which breaks the Electroweak gauge symmetry. The masses of particles are then determined by the strength of their coupling to the Higgs field.

2.2 Beyond the Standard Model

The Standard Model as described above has proven extremely robust through precise experimental testing. There are, however, many remaining questions in physics that cannot be answered within its confines. Some of those not further explored in this thesis include: whether or not there is a quantum theory of gravity that can tie it to the SM, the exact value of the neutrino masses and whether they are Majorana particles (their own antiparticles), and what the cause is of the matter-antimatter

asymmetry in the universe. The fact that these questions are unanswered in the standard model tells us we must search deeper, and test beyond its limits.

2.2.1 Dark Matter

Another currently open question is the nature of dark matter. Astrophysical observations including the dynamics of galaxy clusters [44] and rotational curves of galaxies [38] are not explained under Einstein's theory of gravitation by visible matter alone. Several theories have arisen over time to explain this discrepancy, including that Einstein's theory is not correct at galactic scales, or that these galaxies contain ordinary matter that is somehow unobservable to us.

Most evidence, however, points to the existence of a new type of matter that interacts gravitationally but not electromagnetically with ordinary matter. Perhaps the most clear evidence for this theory comes from observations of the bullet cluster [17], a pair of colliding clusters of galaxies. In such a scenario, with some normal matter and some dark matter in each cluster, the matter would collide and interact, slowing it down, while the dark matter would pass through largely undisturbed. In the case of the bullet cluster, this separation is observed when comparing the distribution of mass in the galaxies measured by gravitational lensing and the distribution of normal matter in the form of galaxy plasma, measured as emitted x-ray radiation. Figure 2.6 shows the observed separation, with gravitational density in blue and x-ray density in pink.

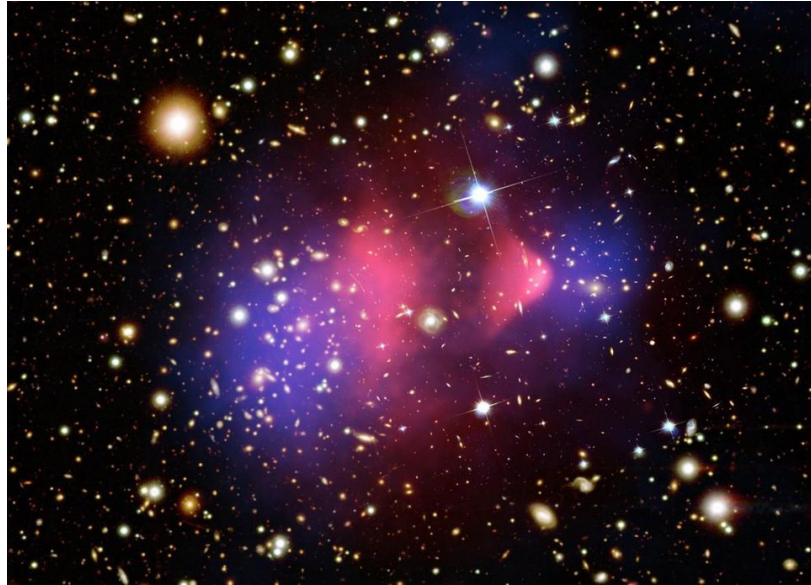


Figure 2.6: The bullet cluster showing separation of x-ray density (pink) and gravitational density (blue).

2.2.2 Dark Higgs Boson Model

This work involves a search for dark matter produced in association with a new hypothetical scalar “dark Higgs” boson s ¹ [20]. In this model the dark matter particle χ is a majorana fermion, who’s mass is generated by a Higgs mechanism in the dark sector. This also generates the new s particle. If the mass of s is less than that of χ then the relic density is set by the process $\chi\chi \rightarrow ss$, followed by the decay of s to standard model particles. The addition of a further paricle, such as a massive Z' boson allows this model to be probed at a collider.

The model proposes that the dark matter particle χ obtains its mass from the vacuum expectation value (vev) w of a new Higgs field S . A new $U(1)'$ gauge group is proposed, under which S carries a charge q_s . As a result, the vev w of S breaks the gauge symmetry, and through this mechanism the mass of the corresponding Z' boson is generated. Additionally, the dark matter particle χ couples to the Z' boson, allowing all particles in the new dark sector to interact. This gives rise to the renormalizable interaction Lagrangian, which can be written in terms of four independent parameters m_χ , $m_{Z'}$, m_s , and g_χ :

¹In this work, s will refer to the dark Higgs boson and not the strange quark, unless otherwise specified

$$\mathcal{L}_\chi = -\frac{1}{2}g_\chi Z'^\mu \bar{\chi} \gamma^5 \gamma_\mu \chi - g_\chi \frac{m_\chi}{m_{Z'}} s \bar{\chi} \chi + 2g_\chi Z'^\mu Z'_\mu (g_\chi s^2 + m_{Z'} s) \quad (2.4)$$

where m_χ is the mass of the dark matter particles, $m_{Z'}$ is the mass of the Z' boson, m_s is the mass of the dark higgs, and g_χ is the dark matter coupling constant.

Additionally, the coupling of the Z' boson to standard model quarks is described by the Lagrangian:

$$\mathcal{L} = -g_q Z'^\mu \bar{q} \gamma_\mu q \quad (2.5)$$

where g_q is the coupling constant between Z' and quarks.

A final free parameter θ is the non-zero mixing angle between the SM Higgs boson and the dark Higgs boson. The dark Higgs obtains its couplings to standard model particles through this mixing, and therefore shares the same standard model decay branching fractions as the SM Higgs boson.

For the analysis described in this work the free parameters are set as:

- $g_\chi = 1$
- $m_\chi = 200 GeV$
- $m_{Z'}$ allowed to vary
- m_s allowed to vary
- $g_q = 0.25$
- $\theta = 0.01$

The values of g_χ and g_q were chosen to facilitate comparison with other LHC searches with similar models, which traditionally use the values selected. The value of θ was chosen to match that of [20]. Its precise value is not relevant to this search, but it is sufficiently large that the dark Higgs decays promptly to standard model states and does not create a displaced vertex. The varied values m_s and $m_{Z'}$ form the parameter space covered by this search.

Chapter 3

The Large Hadron Collider and the ATLAS Experiment

The **Large Hadron Collider (LHC)** is the world's largest and most energetic proton-proton collider. It forms a 27 km circular ring beneath Switzerland and France, with its origin at the **Conseil Européen pour Recherche Nucléaire (CERN)** in Geneva. It began operation in 2008, and since then has collided over 10^{15} particles. The collider houses four major experiments: ALICE, ATLAS, CMS, and LHCb, along with several smaller projects. ALICE (A Large Ion Collider Experiment) studies heavy ion collisions, while LHCb (Large Hardon Collider beauty) specializes in studying the physics of the bottom quark. **ATLAS (A Toroidal LHC ApparatuS)** and CMS (Compact Muon Solenoid) are both general purpose experiments designed to study a wide range of interactions resulting from high-energy proton-proton collisions. This work uses data collected by the ATLAS experiment, and a description of the LHC accelerator and ATLAS detector follow in Sections 3.1 and 3.2.

3.1 The Large Hadron Collider

Built between 1998 and 2008, the LHC [22] began colliding protons in 2010 at a center-of-mass energy of 7 TeV, and most recently from 2015 to 2018 collisions occurred at 13 TeV. Successfully colliding particles at this energy is an immense technical challenge which is achieved by the many technologies of the LHC and its accelerator complex.

In order to reach a beam energy of 6.5 TeV, protons are slowly stepped up through a chain of accelerators before reaching the LHC. They begin their journey as hydrogen

atoms, stripped of their electrons before being accelerated to an energy of 50 MeV by the Linac2 linear accelerator. Following this the Proton Synchrotron Booster (PSB) accelerates them to 1.4 GeV, passing them to the Proton Synchrotron (PS) and the Super Proton Synchrotron to be accelerated to 25 and then 450 GeV. Finally, beams are split into clockwise and counterclockwise directions and injected into the LHC where they are accelerated to their final 6.5 TeV energy. The CERN accelerator complex, including this injection system as well as surrounding experiments is shown in Figure 3.1.

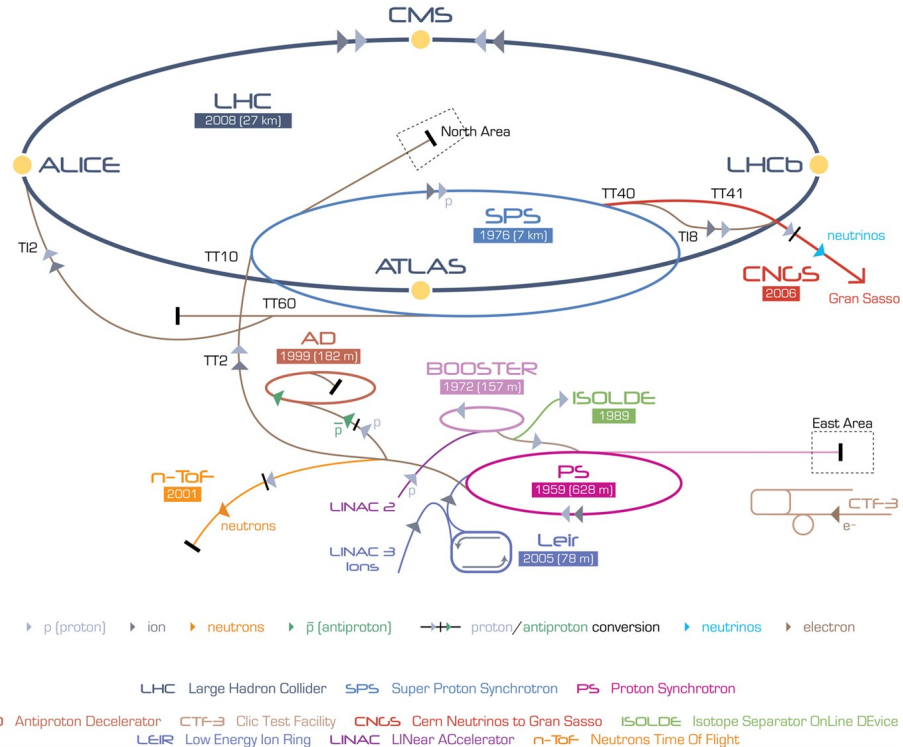


Figure 3.1: Overview of the CERN accelerator complex, including the LHC injector system and surrounding experiments.

The acceleration of the protons is achieved by radio-frequency cavities. These cavities contain a resonant electromagnetic field oscillating at 400 MHz, which is applied to particles passing through. The LHC contains 8 cavities per beam, with each providing a maximum of 2 MV of potential, so each proton can receive up to 16 MeV of energy per lap. As a result it takes millions of laps over a period of around 20 minutes for a proton injected at 450 GeV to reach its collision energy of 6.5 TeV. These RF cavities also serve to keep each beam in bunches of 1.15×10^{11} protons spaced at intervals of just 25 ns.

The crown jewel of LHC technology is its magnets. 1,232 superconducting NbTi dipole magnets kept at 1.9 K, each spanning 14.3 m and weighing 35 tonnes, create an 8.3 Tesla magnetic. This field lies perpendicular to the beam path, bending it to its desired route. The bending dipole magnets are complemented by 392 quadrupole magnets that focus the beams to a small aperture, and many higher-order multipole magnets which provide small beam corrections.

Allong with the collisional energy of the accelerated particles, the other most important measure of a particle acceletator is the luminosity it achieves. **Luminosity** (\mathcal{L}) is used to determine the rate (R) at which a given interaction occurs using:

$$R = \mathcal{L}\sigma \quad (3.1)$$

where σ is the cross-section of the desired interaction. As a result, when searching for rare processes, a obtaining a high luminosity is crucial.

The integrated luminosity, L , gives the total number of interactions over a period of time, and is defined as:

$$L = \int \mathcal{L} dt \quad (3.2)$$

At the LHC, the luminosity is controlled by the number of bunches circulating n_b , the frequency of revolution f_r , $N_{1,2}$ the number of particles in each colliding bunch, and the cross sectional area of the colliding beams. This results in the equation:

$$\mathcal{L} = \frac{f_r n_b N_1 N_2}{4\pi\sigma_x\sigma_y} R_\phi \quad (3.3)$$

where R_ϕ is a geometrical loss factor caused by the beams crossing at an angle, and $\sigma_{x,y}$ are the horizontal and vertical widths of the beams, which are estimated to have a Gaussian profile. The LHC currently has a nominal peak luminosity of $\mathcal{L} = 10^{34} cm^{-2}s^{-1}$.

3.2 The ATLAS Experiment

The ATLAS experiment [5] uses the LHC in combination with the general-purpose ATLAS detector to test a broad range of SM and BSM predictions. Together with the CMS experiment, its greatest achievement to date was the detection and discovery of the SM Higgs boson in 2012 [4].

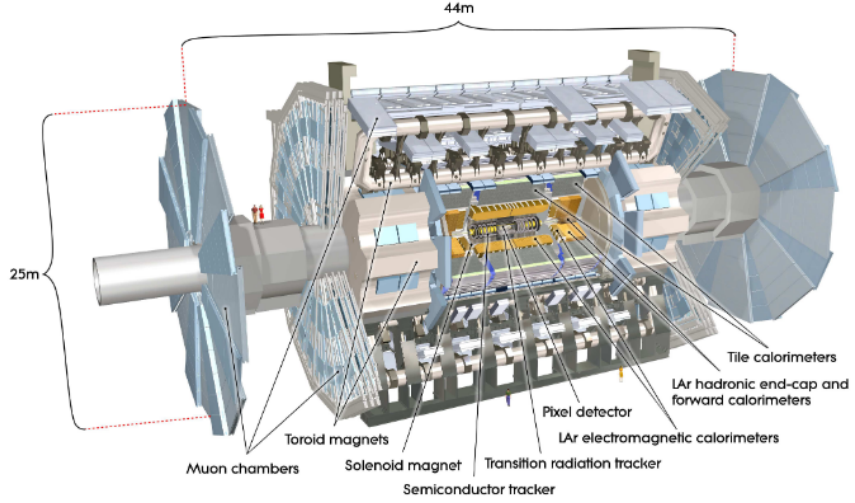


Figure 3.2: A cut-out overview of the ATLAS detector and main components. Diagram from [5].

The ATLAS detector, an overview of which is shown in Figure 3.2, is comprised of several layers, which work in tandem to detect many diverse particles. From innermost to outer-most the layers are:

- the **inner detector**, with excellent angular resolution to track charged particles,
- the **electromagnetic calorimeters**, designed primarily to measure the energy and position of electrons and photons,
- the **hadronic calorimeters** designed to measure the energy and position of hadrons,
- the **muon spectrometer**, to track and measure muons.

When combined with the electronics required to read and trigger on measurements, the entire detector weighs over 7000 t and measures 44 m long by 25 m wide and high. Its barreled shape with end caps covers nearly the full solid angle. The following sections will describe the layout and operations of the ATLAS detector in more detail.

3.2.1 Inner Tracking Detector

The ATLAS inner detector tracks the direction and momentum of charged particles immediately after leaving the interaction point. A 2 T superconducting solenoid surrounds the inner detector, bending charged particles with the Lorentz force, allowing their momentum to be determined from the curvature of their path. Within the inner detector, there are three separate sub-detectors: the **Pixel Detector**, the **Semiconductor Tracker (SCT)**, and the **Transition Radiation Tracker (TRT)**. A cutout view of the detector is shown in Figure 3.3.

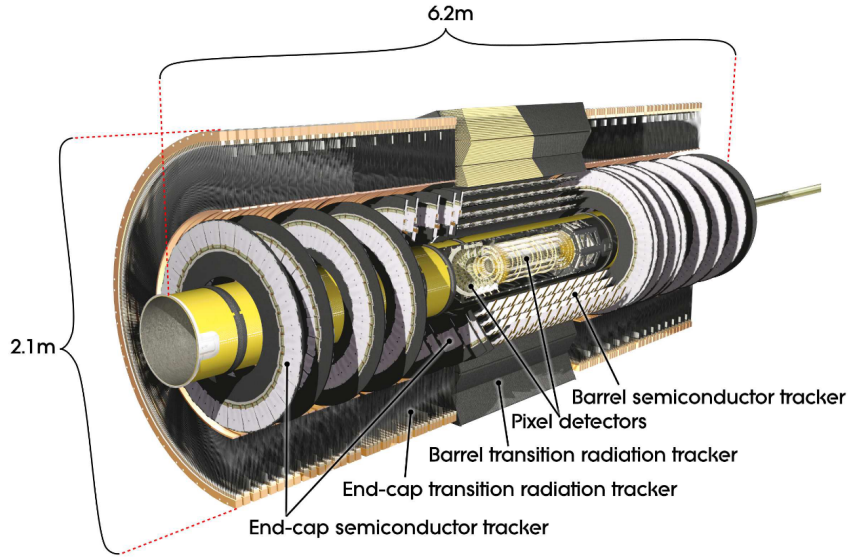


Figure 3.3: A cut-out view of the ATLAS inner detector. Diagram from [5].

The Pixel Detector consists of an array of 1744 pixel sensors, each containing 47232 silicon pixels, mostly measuring $50 \times 400 \mu\text{m}^2$. They are arranged into three cylindrical layers in the barrel and three disk-shaped layers on each end. The high granularity of these detectors ensures strong angular resolution, providing precise measurements of vertex location and track momentum. Notably, this detector must be very radiation-hard in order to maintain performance over the detector lifespan in an area that receives an immense radiation dose from the high particle flux.

Though it would be desirable, it would not be feasible to extend the high-resolution pixel detector because of the high cost and signal readout volume. As a result, in the SCT the point-like pixels are extended into silicon strip detectors, which are laid in pairs at an angle of 40 mrad to each other to allow measurements

in two dimensions. The SCT is made up of four concentric cylindrical layers in the barrel and two disk-shaped layers on each end-cap.

The TRT is the final component of the component of the inner detector. It consists of approximately 300000 drift tubes filled with majority Xenon gas, with the walls kept at -1.5 kV and a central wire at ground. When particles pass through the tubes, the gas is ionized and the resulting electrons drift to the centre where the signal is amplified. Additionally, the gaps between TRT straws are filled with polymer fibres (in the barrel) or foils (in the end caps). As a result, highly relativistic particles create transition radiation at the material interfaces, which aids with electron identification.

3.2.2 Calorimeters

The ATLAS calorimeter system measures the energy and positions of both charged and neutral particles after they leave the inner detector. In addition to measuring the energy of particles, the calorimeters must contain enough material to stop the vast majority of particles (with the exception of muons and undetected neutrinos) from reaching the muon spectrometers. To achieve this, high-density passive layers interact with passing particles and cause them to decay into showers, dispersing their energy. These layers are interleaved with active layers that detect the decaying showers to measure particle energy.

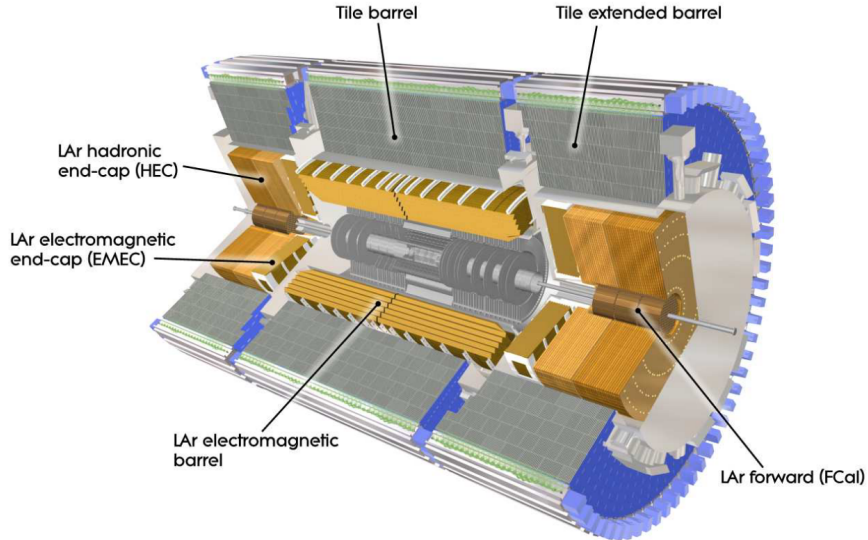


Figure 3.4: A cut-out view of the ATLAS calorimeter system. Diagram from [5].

The ATLAS calorimeters can be categorized into electromagnetic (EM) calorimeters which measure the energy of electrons and photons and hadronic calorimeters which primarily measure the energy of hadrons. ATLAS uses a combination of two different calorimeter technologies to form these detectors. In the end-cap and forward regions Liquid Argon (LAr) is used as the active layer in both the hadronic and EM calorimeters, while in the barrel region plastic scintillating tiles are employed in the hadronic calorimeter. Figure 3.4 depicts the layout of the ATLAS calorimeter system.

Electromagnetic calorimeters

The electromagnetic LAr calorimeter lies just outside the solenoid surrounding the inner detector. Layers of lead are used as the passive material. In the lead, electrons and photons interact with the closely spaced atoms, initiating a cascading shower of decays. The charged electrons in the shower pass through the active layers and ionize the LAr inside. The electrons and ions then drift across the 2 kV difference to opposite electrodes, where they are amplified into an electrical signal.

Like the inner detector, the LAr EM calorimeter can be divided into an **Electromagnetic Barrel (EMB)** calorimeter and two **Electromagnetic End-Cap (EMEC)** calorimeters. In the barrel region, the layers are placed together in a folded accordion-like geometry to create uniformity and allow easy electronic readout. The barrel and end-cap regions are 53 cm and 63 cm thick respectively, and cover a minimum of 22 and 24 radiation lengths (X_0), keeping shower leakage to a minimum.

Hadronic Calorimeters

In the end cap regions, the **Hadronic End-Cap (HEC)** calorimeter shares a similar design to the EM LAr calorimeters, but with copper as the passive absorbing material between active layers. In the barrel region, the hadronic calorimetry is performed by the **Tile Calorimeter** with plastic scintillators as the active detectors. Particle showers passing through the plastic tiles produce scintillating light, which is directed to photomultipliers to be converted to an electrical signal. In the tile calorimeter, steel is the passive material laid between active layers. The depth of the combination of electromagnetic and hadronic calorimeters is important to prevent particles from punching through to the background-sensitive muon spectrometer. The total thickness, including supporting materials, is approximately 11 interactions lengths,

which keeps punch-through below the levels of irreducible backgrounds in the muon spectrometer and also ensures an accurate measurement of E_T^{miss} as very little energy escapes measurement.

The final calorimeter in the ATLAS detector is the **Forward Calorimeter (FCal)**, located nearest the beam path. It has three layers of passive absorbing metals: an inner copper layer optimized for electromagnetic measurements and two outer tungsten layers to measure hadronic interactions. It too employs liquid argon as the active material, this time in a matrix of longitudinal channels parallel to the beam line.

3.2.3 Muon Spectrometers

After the calorimeters have stopped the vast majority of particles exiting the interaction point, muons and neutrinos remain undetected. The ATLAS experiment does not directly detect neutrinos, and instead reconstructs them from missing transverse momentum, but muons are measured by the muon spectrometer. A diagram of the muon system is shown in Figure 3.5. The centerpiece of this system is an arrangement of three air-core toroidal magnets, a barrel toroid and two end-cap toroids. Each toroid consists of eight coils in loops in a radially symmetric pattern around the beam line. Together they form a 4 T magnetic field to bend muons.

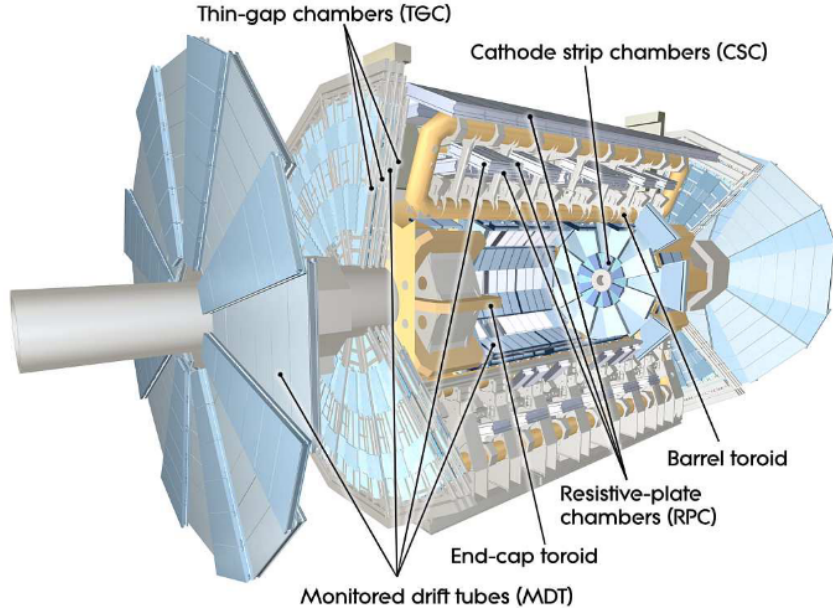


Figure 3.5: A cut-out view of the ATLAS muon spectrometer system. Diagram from [5].

Four different detector types are used to measure the muons. **Monitored Drift Tubes (MDTs)** are pressurized gas drift tubes that collect ionized electrons to measure track coordinates in the bending direction of the magnetic field. They are supplemented by finer-grained and more radiation-hard **Cathode Strip Chambers (CSCs)** at $|\eta| > 2$. **Resistive Plate Chambers (RPCs)** and **Thin Gap Chambers (TGCs)** measure the muon track coordinates in the direction orthogonal to the magnetic bending direction, and are also used by the trigger system to provide bunch-crossing identification and p_T thresholds.

3.2.4 Trigger and Data Acquisition

The ATLAS detector can see as many as 1.7 billion proton-proton collisions per second, but to save and process all of the information from each collision would require a prohibitive amount of readout electronics, computing power, and storage space. Instead, the trigger system quickly selects events based on key observables to slim down the data. On the detector itself, the **Level-1 (L1) trigger** uses custom electronics within the detector, and works with reduced granularity information from the muon chambers and calorimeters to select potentially interesting events with high- p_T objects or high E_T^{miss} . The detector readout systems can handle a maximum acceptance rate of 100 kHz from the L1 trigger. The **Level 2 (L2) trigger** is outside the detector and uses traditional computing resources. It takes regions of interest where the L1 trigger finds interesting objects and reconstructs them more fully to further reduce the event rate below 3.5 kHz. Together with the L2 trigger, the **event filter** forms the second half of the **High-Level Trigger (HLT)**. At this stage, events are fully reconstructed before being further filtered to a rate of approximately 200 Hz to be analyzed offline.

Chapter 4

Analysis Preparation

4.1 Signal Model

This work concerns a search for dark matter produced in association with a dark Higgs boson as described in Section 2.2.2. The dark Higgs boson then decays to standard model particles with the same branching ratios as a standard model Higgs boson of variable mass, shown in Figure 4.1. At low s mass this is dominated by a decay to a pair of b quarks, which has previously been explored by reinterpreting the ATLAS search for dark matter produced in association with a standard model Higgs boson decaying to $b\bar{b}$ in [37]. At s masses above 160 GeV , however, the decay to a pair of W bosons, shown in Figure 4.2 becomes kinematically available on-shell. Even slightly below this threshold, s decays to WW are the dominant process. The pair of W bosons decay rapidly, and are not detected as final state particles by the ATLAS detector. Instead, they each decay either to hadronic ($q\bar{q}$) or leptonic ($l\nu$) final states. A search in the fully hadronic channel, with both W decaying to $q\bar{q}$ is complete (see [7]), and this work focuses on the semileptonic decay channel with one $W \rightarrow q\bar{q}$ and one $W \rightarrow l\nu$. When both analyses are complete, the results will be statistically combined.

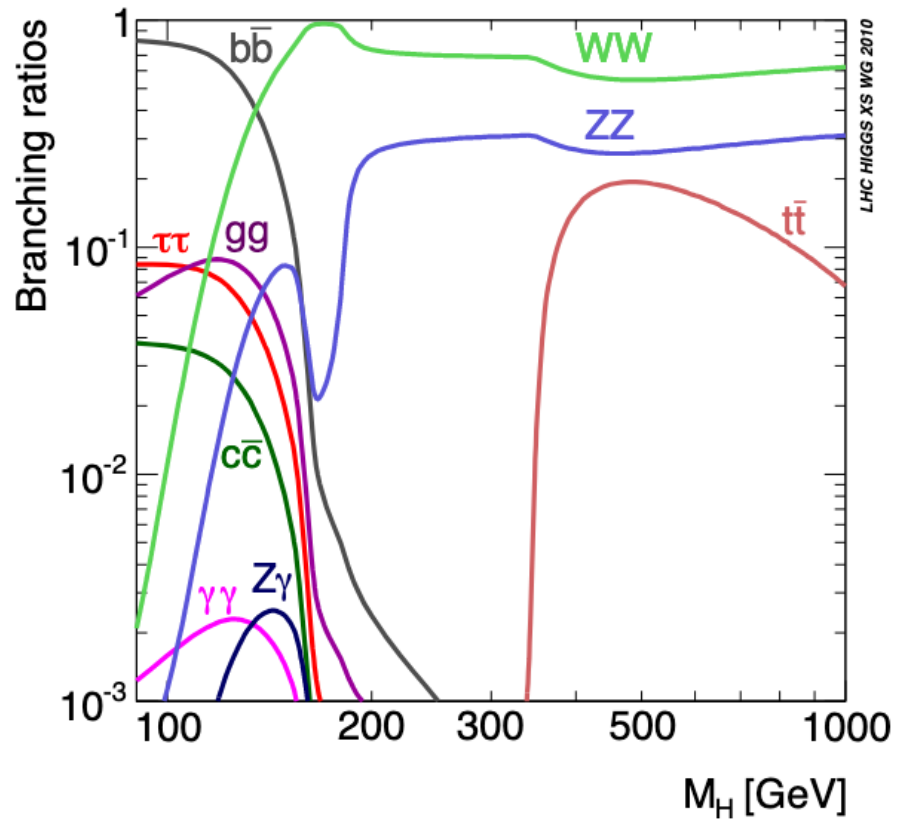


Figure 4.1: Branching fractions for a SM Higgs boson as a fraction of the Higgs boson mass [19].

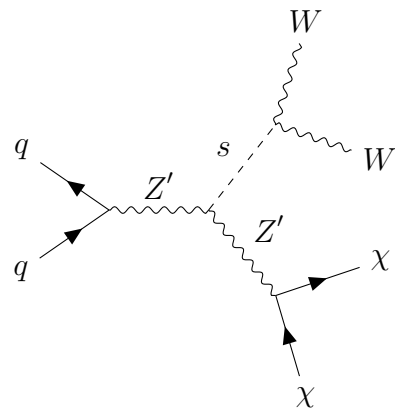


Figure 4.2: DH Decay

In the ATLAS detector this signal signature will be characterized by a single lepton in the final state from the $W \rightarrow l\nu$ decay, along with a pair of jets from the

$W \rightarrow q\bar{q}$ decay and a strong missing transverse momentum signature from the dark matter particles and neutrino.

4.2 Monte Carlo Production and Data

In order to search for a signal such as the one described above, it is necessary to form a prediction which can be compared with data from the ATLAS detector. In order to achieve this, simulated data is produced using Monte Carlo (MC) generators according to standard model predictions. This represents “background” data, or what we would expect to see if the signal process did not exist. On top of this, signal MC samples are produced according to the signal model. Then, after isolating for an area of phase space that would be rich in signal events, the ATLAS data can be compared with the simulated data with or without signal events to make statistical conclusions about the likelihood of their existence. The following sections will detail the MC and data samples produced for this analysis.

4.2.1 Signal MC

Signal samples are produced using the model and parameter choices outlined in Section 2.2.2. They are produced by calculating the hard process cross-section at leading order (LO) using MADGRAPH5_aMC@NLO 2.7.2 [10] interfaced with PYTHIA8 8.230 [40] for parton shower modelling. The CKKW-L [34] procedure with a matching scale of $\min(m_s/4, 40 \text{ GeV})$ is used to prevent overlap between the cross-section matrix element and parton shower. Two separate signal grids were produced, with the second covering an expanded parameter space. In the first, MADGRAPH5_aMC@NLO is used with the NNPDF30 LO PDF set with $\alpha_s = 0.13$ [12], while in the second MADGRAPH5_aMC@NLO is used with the NNPDF23 LO PDF set with $\alpha_s = 0.13$ and LO QED [13]. The signals studied span a parameter space in m_s and $m_{Z'}$ with samples produced at the mass points shown in Figure 4.3. After production, it was found that the second set of samples did not use the ATLAS recommended PDF Set, which is in fact the NNPDF30 NLO PDF set with $\alpha_s = 0.118$. When used, the weights of events in these samples are therefore scaled to match cross-sections derived from the recommended PDF set.

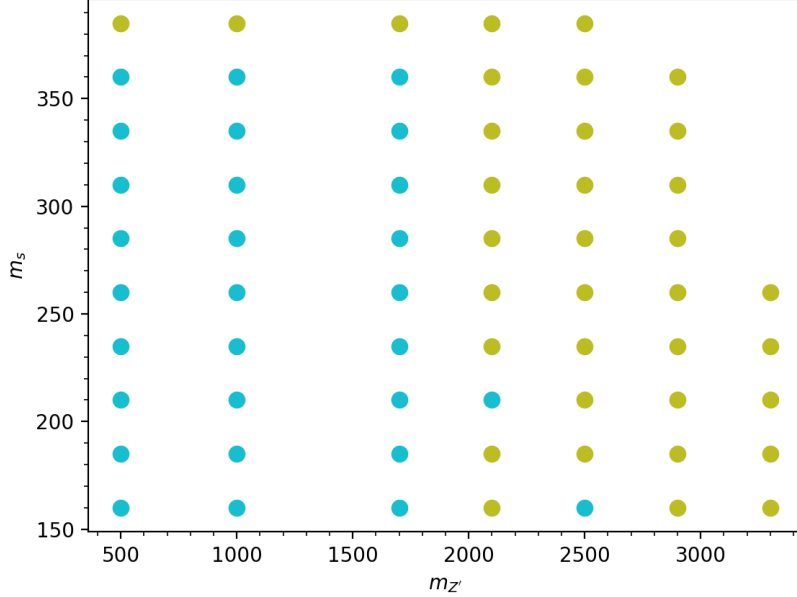


Figure 4.3: Signal point locations in m_s vs. $m_{Z'}$ parameter space. Blue points represent the original signal grid while green points are added in the second signal grid

4.2.2 Background MC

The dominant SM backgrounds for this analysis are:

- $W + \text{jets}$ events a single W boson and 1 or more jets,
- $t\bar{t}$ events with a top and anti-top pair,
- and *Diboson* events with a pair of vector bosons

Additionally, $Z + \text{jets}$ and single-top quark (stop) events make non-negligible background contributions. All background contributions are estimated using MC simulated data, and the $W + \text{jets}$ and $t\bar{t}$ backgrounds are further constrained using data-driven control regions.

$V + \text{jets}$ and diboson

Like signal, two distinct sets of $W + \text{jets}$ and $Z + \text{jets}$ ($V + \text{jets}$) background samples are used. The samples are similar in that they are simulated with the SHERPA v2.2 MC

generator [14] with up to two additional parton emissions at NLO or four additional parton emissions at LO accuracy [11][24]. Merging of parton showers with matrix elements is achieved using CKKW matching with the MEPS@NLO prescription extending this to NLO [31]. The NNPDF30 NNLO PDF set is used [12].

The difference is that first samples are produced using SHERPA v2.2.1, and the second with SHERPA v2.2.10. As well, additional statistics-enhanced $W+jets$ samples are added to the second set with $m_W > 120 \text{ GeV}$ [24]. This greatly increases the number of simulated events in this small section of phase space that is important to this analysis. Overlap removal in m_W is performed between these mass-enhanced samples and the other $W+jets$ samples.

Diboson samples are similarly generated with only a single set using either SHERPA v2.2.1 or 2.2.2 depending on the process, and CKKW matching again used to merge parton shower and matrix element simulation.

$t\bar{t}$ and single-top

MC samples for the $t\bar{t}$ and single-top standard model background process are modelled using the POWHEGBOX v2 [9] generator, which gives matrix elements at NLO in the strong coupling constant α_s . This uses the NNPDF30 NLO PDF set [12]. Like for signal samples, this is combined with PYTHIA8 8.230 [40] for parton shower modelling using the NNPDF23 LO PDF set [13].

4.2.3 Data

This analysis uses data for the full Run-2 period, from 2015-2018, with individual runs selected using the good runs lists:

- `data15_13TeV.periodAllYear_DetStatus-v89-pro21-02_Unknown_PHYS_StandardGRL_All_Good_25ns.xml`
- `data16_13TeV.periodAllYear_DetStatus-v89-pro21-01_DQDefects-00-02-04_PHYS_StandardGRL_All_Good_25ns.xml`
- `data17_13TeV.periodAllYear_DetStatus-v99-pro22-01_Unknown_PHYS_StandardGRL_All_Good_25ns_Triggerno17e33prim.xml`
- `data18_13TeV.periodAllYear_DetStatus-v102-pro22-04_Unknown_PHYS_StandardGRL_All_Good_25ns_Triggerno17e33prim.xml`

This results in a total integrated luminosity of 138.5 fb^{-1} .

MC Scaling to Match Data Luminosity

The events in MC simulated samples above must be re-weighted in order to match the total integrated luminosity of the ATLAS data used. In order to achieve this the weight of each MC event is given by:

$$weight = \frac{\sigma \times (138.5 \text{ fb}^{-1}) \times (k) \times (filt_{eff}) \times (GenWeight) \times (wf)}{\sum_{Events \text{ in } AOD} GenWeight} \quad (4.1)$$

where

- σ is the cross section for the simulated process in fb,
- k is the k-factor, which corrects for the omission of higher-order terms in event generation,
- $filt_{eff}$ is the filter efficiency, the fraction of events passing any filters applied during event generation to emphasize a certain phase space,
- GenWeight is the generator weight from MC production,
- and wf is a set of weight factors given by:

$$wf = EleWeight \times MuoWeight \times JetWeightJVT \times prwWeight \quad (4.2)$$

where the various weights apply small corrections from the generation and reconstruction process.

4.3 Object Definition

Once events have been simulated or produced in the ATLAS detector, the information contained in them must be reconstructed into objects which can be analyzed. These objects represent particles or groups of particles and are used to fully or partially reconstruct events and search for signal signatures. The following section will detail the definition of physics objects used in this analysis.

4.3.1 Muons

From the ATLAS detector, muons are reconstructed from measurements in the Inner Detector and the Muon Spectrometer. For this analysis, two different definitions of

muons are used. “*Baseline*” muons use a slightly less selective reconstruction than “*signal*” muons, which are designed for high purity. *Baseline* muons are selected using the *Loose* identification criteria as defined in [6], which is designed to maximize efficiency. *Signal* muons, meanwhile, use the *Medium* identification criteria, and must also be isolated from other signatures according to the *Tight* track-based working point with variable radius dependent on p_T . Additionally, all muons are rejected if they are considered “badly reconstructed” or “cosmic”, and track-to-vertex association cuts are applied. Table 4.1 summarizes the muon selection criteria.

Table 4.1: Muon object definition criteria

Criterion	Baseline Muon	Signal Muon
Identification	Loose	Medium
Isolation	-	<code>TightTrackOnly_VarRad</code>
Pseudorapidity	$ \eta < 2.7$	$ \eta < 2.5$
p_T	$p_T > 7 \text{ GeV}$	$p_T > 7 \text{ GeV}$
Veto	Cosmic or Bad	Cosmic or Bad
Track-to-vertex association	$ d_0/\sigma_{d_0} < 3$ $ \Delta z_0^{\text{BL}} \sin \theta < 0.5 \text{ mm}$	$ d_0/\sigma_{d_0} < 3$ $ \Delta z_0^{\text{BL}} \sin \theta < 0.5 \text{ mm}$

4.3.2 Electrons

Electrons are reconstructed by associating energy deposits in the EM calorimeter with tracks in the inner detector. Like for muons, two different definitions are used, with “*baseline*” electrons requiring slightly less selective criteria than “*signal*” electrons. *Baseline* and *signal* electrons are selected using a likelihood-based identification described in [1]. *Signal* electrons require the medium identification criteria, while *baseline* electrons require the loose criteria as well as a hit in the innermost layer of the pixel detector. Additionally, *baseline* and *signal* electrons must both satisfy the fixed-cut *Loose* isolation requirement. Like for muons, track-to-vertex association cuts are also applied. Table 4.2 summarizes the electron selection criteria.

Table 4.2: Electron object definition criteria

Criterion	Baseline Electron	Signal Electron
Identification	LooseAndBLayerLLH	MediumLLH
Isolation	FCLoose	FCLoose
Pseudorapidity	$ \eta < 2.47$	$ \eta < 2.47$
p_T	$p_T > 7 \text{ GeV}$	$p_T > 7 \text{ GeV}$
Track-to-vertex association	$ d_0/\sigma_{d_0} < 5$ $ \Delta z_0^{\text{BL}} \sin \theta < 0.5 \text{ mm}$	$ d_0/\sigma_{d_0} < 5$ $ \Delta z_0^{\text{BL}} \sin \theta < 0.5 \text{ mm}$

4.3.3 Small-radius ($R = 0.4$) Jets

In this analysis, small-R jets are used to reconstruct the hadronically decaying W boson in some analysis regions. Small-R jets are built using particle-flow objects [2] clustered with the anti- k_t algorithm [15] with radius $R = 0.4$. Following reconstruction, only jets with $p_T > 20 \text{ GeV}$ and $|\eta| < 2.5 \text{ GeV}$ are used for analysis. As well, in order to suppress noise from pileup, the jet vertex tagger [41] is applied with the Tight working point.

***b*-jets**

For this analysis, it is also beneficial to identify jets originating from bottom (b) quarks. In signal regions these jets are vetoed to reduce background. This is performed using the **DL1r** [32] b-tagging algorithm, which employs a deep-learning neural network. A 77% efficient tagger working point is used. Table 4.3 summarizes $R = 0.4$ jet criteria and tagging.

Table 4.3: $R = 0.4$ jets object definition criteria

Criterion	Requirement
Collection	AntiKt4EMPFlowJets
Pseudorapidity	$ \eta < 2.5$
p_T	$p_T > 20 \text{ GeV}$
Jet-Vertex-Tagger WP	Tight
<i>b</i> -tagger	DL1r

4.3.4 Track-Assisted-Reclustered Jets

Track-Assisted-Reclustered (TAR) jets [42] are used in this analysis to reconstruct hadronically decaying W boson candidates in some regions. $R = 0.2$ jets, constructed with the anti- k_t algorithm [15] from locally calibrated topological clusters [8] are used as input for building TAR Jets. As well, the TAR algorithm uses tracks fulfilling quality criteria outlined in Table 4.4. The TAR building process involves constructing large-R jets from the constituent small-R jets. Tracks are then matched with the input jets and rescaled using the p_T of the matched jets. The kinematic properties of the TAR jets are then calculated from the constituent $R = 0.2$ jets, while the jet substructure variables are calculated from the constituent tracks. Figure 4.4 shows a visual summary of the base TAR algorithm, and the following steps outline the algorithm in more detail:

- Tracks and calibrated anti- k_t $R = 0.2$ jets are chosen as input to the algorithm.
- The anti- k_t $R = 0.2$ jets are reclustered using the anti- k_t algorithm into $R = 1.0$ jets and trimmed using the p_T fraction $f_{cut} = 0.05$.
- Input tracks are matched to $R = 0.2$ jets if possible using ghost association.
- Tracks which remain unassociated are matched to the nearest anti- k_t $R = 0.2$ jet within $\Delta R < 0.3$
- The p_T of each track is rescaled using the p_T of the jet to which it is matched using the equation:

$$p_T^{\text{track, new}} = p_T^{\text{track, old}} \times \frac{p_T^{\text{subjet } j}}{\sum_{i \in j} p_T^{\text{track } i}}, \quad (4.3)$$

where j is the $R = 0.2$ subjet that the track being rescaled is matched with, and the index i runs over all tracks matched to that subjet. This rescaling accounts for the missing neutral momentum, which is measured at calorimeter level but is not present at tracker level.

- Finally, jet substructure variables and m^{TAR} are calculated using the rescaled matched tracks.

The parameters of the TAR algorithm used are summarized in Table 4.4.

Table 4.4: TAR jet reconstruction parameters

	Loose quality
Input track selection	$p_T > 0.5 \text{ GeV}$ $ \eta < 2.5$ $ d_0 < 2 \text{ mm}$ $ \Delta z_0^{\text{BL}} \sin \theta < 3.0 \text{ mm}$
Track-to-vertex association	
Input jet selection	$R = 0.2$ topo jets $p_T > 20 \text{ GeV}$ $ \eta < 2.5$
Reclustering radius	$R = 1.0$
TAR jet p_T	$p_T^{\text{TAR}} > 100 \text{ GeV}$
Trimming radius	$R = 0.2$
Trimming p_T fraction	$f_{\text{cut}} = 0.05$
Track-to-jet association	$\Delta R(\text{jet}, \text{track}) < 0.3$

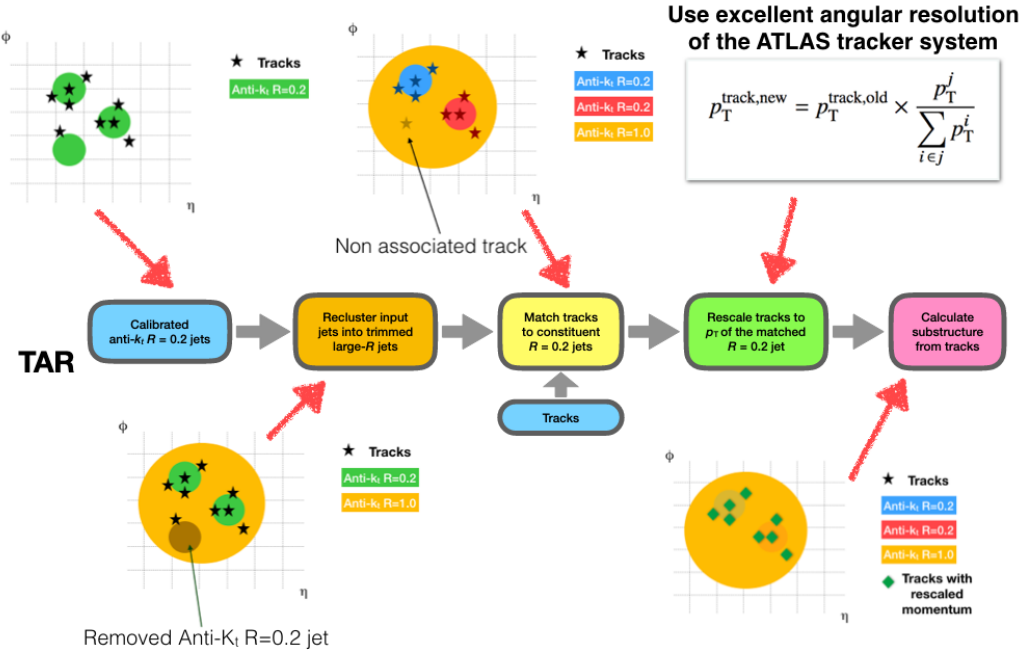


Figure 4.4: A visual summary of the TAR Jet algorithm.

4.3.5 Missing Transverse Momentum (E_T^{miss})

In the ATLAS detector, the beams collide directly along the longitudinal axis. As a result of the conservation of momentum, all decay products from the collision should

thus have a total transverse momentum of 0. Using this information, missing transverse momentum (E_T^{miss}) can be used to represent undetected objects. In the signal model described in Section 2.2.2 both the neutrino from the leptonically decaying W -boson and the dark matter would not be directly detected in ATLAS. It is impossible to disentangle these objects, and they are reconstructed together using E_T^{miss} . E_T^{miss} is calculated for this analysis using baseline electrons and muons as described in Sections 4.3.2 and 4.3.1 as well as $R = 0.4$ jets with the **Tight** working point applied. No photons or τ -leptons are included in the calculation. An additional soft term, which is calculated from tracks not associated with the reconstructed objects, is also added.

E_T^{miss} Significance

The significance of the E_T^{miss} measurement is also assessed using the object-based E_T^{miss} significance \mathcal{S} . It is calculated as described in [35] from a combination of the uncertainties on the reconstructed objects and soft term used to calculate E_T^{miss} , as well as a pileup correction. A high \mathcal{S} indicates a higher degree of confidence that the E_T^{miss} measurement of an event comes from an unseen object rather than from particle mismeasurement.

Chapter 5

Analysis

After data and simulated data samples are produced and physics objects are defined and reconstructed within them, the resulting information can be analyzed to search for evidence of the existence of new physics.

This thesis focuses on the design of the most sensitive “merged” signal region as well as the addition of a control region to constrain the $t\bar{t}$ background contribution. Other analysis regions are described in more brief detail in order to provide context to decision-making and a fuller picture of the analysis.

5.1 Cut and Count Analysis

This analysis uses the “cut and count” strategy to search for evidence of the signal model. In a cut and count analysis a set of selection criteria are chosen which slice or “cut” the data according to various event variables, such as the amount of missing transverse momentum. These selection criteria are chosen in order to maximize the expected number of signal events and minimize the expected number of standard model background events entering the region based on the MC simulated data. While designing the selection criteria, real ATLAS data is blinded to avoid biasing the selection. The final area of phase space defined by the selection criteria is known as the “signal region”. At the culmination of an analysis, the real ATLAS data can be compared with the simulated MC data and a statistical conclusion can be reached about the likelihood of the existence of the signal model.

In order to improve the accuracy and uncertainty of the predicted standard model background a “control region” may also be used. This is a region orthogonal to the

signal region which is designed to have similar kinematic properties but be more pure in one or more standard model backgrounds and much less rich in expected signal events. In this region the number of MC simulated background events and ATLAS data events are compared. Their ratio can therefore provide additional information to correct and constrain the expected number of background events in the signal region.

5.2 Analysis Strategy

In this analysis there are two analysis channels which are combined statistically during fitting. These channels are distinguished by the reconstruction of the dijet system from the hadronically decaying W boson, and are named the “merged” channel and the “resolved” channel. In the “merged” channel the dijet system is reconstructed by a single $R = 1.0$ TAR jet, which generally means it is more boosted with the s decay products closer together. In the less-boosted “resolved” channel the dijet system is reconstructed by a pair of $R = 0.4$ jets. Figure 5.1 provides a visual demonstration of this difference. In each analysis channel there are three analysis regions: the semileptonic signal region, a control region designed to constrain the $t\bar{t}$ background, and a control region designed to constrain the $W + \text{jets}$ background. To ensure “merged” and “resolved” regions are orthogonal, an event recycling strategy is employed where only events failing the selection for all “merged” regions are considered for selection in “resolved” regions.

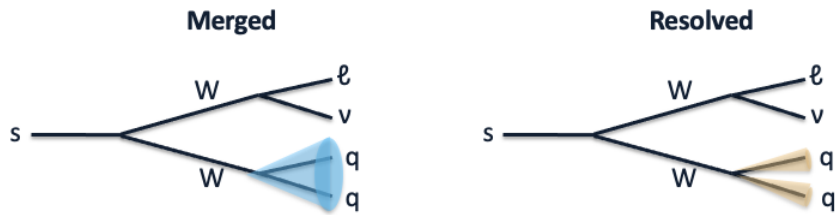


Figure 5.1: Schematic representation of the differing reconstruction technique between merged and resolved regions.

5.3 Merged Signal Region

Something here??

5.3.1 Signal and Background Characterization

The first step towards defining signal region selection criteria was to characterize the signal and background events while searching for exploitable differences. Event characteristics explored include the relative positions of analysis objects, the transverse momenta and masses of analysis objects, along with various jet substructure variables. Figure in A

5.3.2 TAR Jet Lepton Disentanglement

Reconstructing the hadronically decaying W-boson as accurately as possible is key in this analysis. As a result, it was given special attention, especially in the more sensitive merged channel. In this channel, the W is reconstructed by a single $R = 1.0$ TAR jet. Due to the boosted nature of the s -decay, however, the leptonically decaying W often lies very near to this jet. As a result the lepton often overlaps the TAR jet, which can lead to difficulty in jet reconstruction.

In order to resolve this difficulty, modifications are made to the TAR jet building process to disentangle overlapping leptons. Input tracks and jets that are considered likely to be attributable to a final state lepton and not the hadronic W decay are removed. First, tracks associated with a baseline electron or muon are removed from the input track collection. Additionally, any anti- k_t $R = 0.2$ jet overlapping with a baseline electron (defined here as having $\Delta R(\text{lep}, \text{jet}) < 0.2$) is removed prior to reclustering into $R = 1.0$ jets. $R = 0.2$ jets overlapping muons are not removed, as muons do not leave a calorimeter signature and are therefore unlikely to fake hadronic activity. This results in the following updated TAR jet building algorithm, where steps with a (*) are added to disentangle leptons:

- Tracks and calibrated anti- k_t $R = 0.2$ jets are chosen as input to the algorithm.
- Tracks associated with a baseline muon or electron are removed from the input collection (*).
- anti- k_t $R = 0.2$ jets overlapping with a baseline electron ($\Delta R < 0.2$) are removed from the input collection (*).
- The remaining anti- k_t $R = 0.2$ jets are reclustered using the anti- k_t algorithm into $R = 1.0$ jets and trimmed using the p_T fraction $f_{cut} = 0.05$.

- Input tracks are matched to $R = 0.2$ jets if possible using ghost association.
- Tracks which remain unassociated are matched to the nearest anti- k_t $R = 0.2$ jet within $\Delta R < 0.3$
- The p_T of each track is rescaled using the p_T of the jet to which it is matched using the equation:

$$p_T^{\text{track, new}} = p_T^{\text{track, old}} \times \frac{p_T^{\text{subjet } j}}{\sum_{i \in j} p_T^{\text{track } i}}, \quad (5.1)$$

where j is the $R = 0.2$ subjet that the track being rescaled is matched with, and the index i runs over all tracks matched to that subjet. This rescaling accounts for the missing neutral momentum, which is measured at calorimeter level but is not present at tracker level.

- Finally, jet substructure variables and m^{TAR} are calculated using the rescaled matched tracks.

In order to study the potential benefit of lepton-disentanglement, near-identical ntuple samples of signal MC samples were produced with one implementing disentanglement and the other not. The mass of the reconstructed jets in the two samples were then compared in a region where an electron overlaps the $R = 1.0$ TAR Jet ($\Delta R(e, R=1.0\text{TAR}) < 1$), to determine how well the W boson mass is reconstructed in this case. Figure 5.2 demonstrates the improvement in mass resolution achieved by disentangling leptons from TAR jets. A clearly enhanced resolution in the TAR jet mass peak around the W mass is visible for the disentangled jets. This significantly improves sensitivity in the merged electron signal region.

An additional study was undertaken to compare the performance of building the TAR jets from constituent anti- k_t $R = 0.4$ jets rather than anti- k_t $R = 0.2$ jets. In the electron region it was found that for high s mass, W mass resolution performance was similar between the two methods, but for low s mass, using anti- k_t $R = 0.4$ jets significantly improved resolution around the W mass. In the muon region few significant differences were observed. Figure 5.3 shows a comparison of the TAR jet mass distribution built from anti- k_t $R = 0.4$ and anti- k_t $R = 0.2$ for select signal points in a signal enriched region with 1 electron and $\Delta R(e, R = 1.0 \text{ TAR}) < 1$ and $m_T(\ell, E_T^{\text{miss}}) > 150 \text{ GeV}$.

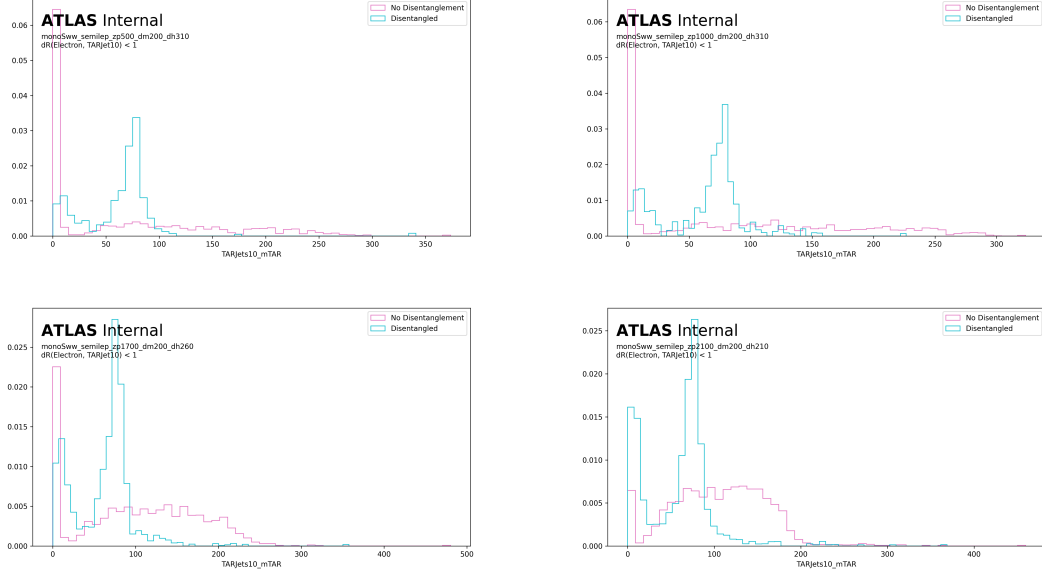


Figure 5.2: Normalized $R = 1.0$ TAR jet mass distributions with and without lepton disentanglement applied for several representative signal points

5.3.3 Merged Signal Region Optimization

Asimov Significance

The “merged” signal is optimized in order to maximize the expected Asimov discovery significance Z given by:

$$Z = \left[2(s + b) \left(\ln \left[\frac{(s + b)(b + \sigma_b^2)}{b^2 + (s + b)\sigma_b^2} \right] - \frac{b^2}{\sigma_b^2} \ln \left[1 + \frac{\sigma_b^2 s}{b(b + \sigma_b^2)} \right] \right) \right]^{\frac{1}{2}} \quad (5.2)$$

where b is the expected total number of background events, s is the expected total number of signal events, and σ_b is the uncertainty on the expected total number of background events [18]. For a given set of selection criteria and signal mass point, this metric can be calculated from the MC simulated data by applying the criteria and counting the signal and background events and computing their uncertainties. It provides a metric to assess the expected sensitivity of the signal region to signal events.

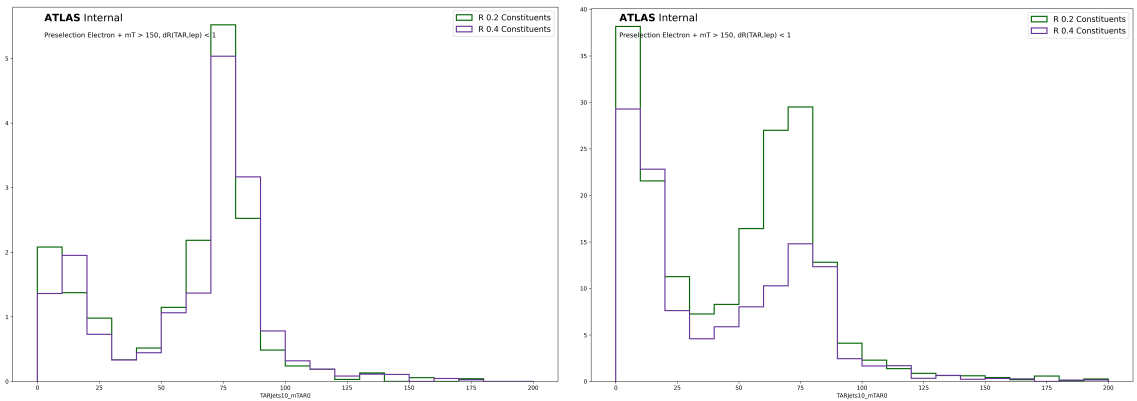


Figure 5.3: TAR jet mass distributions for two representative signal points compared with constituent anti- k_t $R = 0.4$ vs. anti- k_t $R = 0.2$ jets. Left: sample signal point at $(m_s, m_{Z'}) = (310, 500) \text{ GeV}$. Right: sample signal point at $(m_s, m_{Z'}) = (160, 1700) \text{ GeV}$

Optimization Approach

In order to optimize the signal region selection a combination of an iterative visual approach and a computational approach were used. Visually, the distributions of analysis variables were studied to find areas of good discrimination, where a cut placement might improve sensitivity. A list of possible cuts in these areas of discrimination was then compiled to form a basis for the computational approach. In order to determine the optimal combination of these possible cuts, a script was written to test all possible combinations (order of 10^6) while computing the expected asimov significance of each. When calculating significance during optimization in addition to statistical uncertainty, a flat 20% systematic uncertainty on the number of background events was applied to more realistically reflect the expected situation. Different signal points in the m_s - $m_{Z'}$ plane have different kinematic properties and therefore have different optimal selection. As a result, four signal points at the edge of the search sensitivity were selected for optimization:

- $(m_s, m_{Z'}) = (310 \text{ GeV}, 500 \text{ GeV}),$
- $(m_s, m_{Z'}) = (335 \text{ GeV}, 1000 \text{ GeV}),$
- $(m_s, m_{Z'}) = (285 \text{ GeV}, 1700 \text{ GeV}),$
- and $(m_s, m_{Z'}) = (210 \text{ GeV}, 2100 \text{ GeV}).$

The cut combination with the highest mean expected Asimov significance over these four points was considered optimal. In early iterations of optimization, the number of signal events selected using the optimal selection criteria was undesirably low. As a result an additional requirement was implemented forcing the chosen criteria to maintain an expected yield of 15 expected signal events in the “merged” signal region.

In order to minimize over-tuning the optimization on single events or statistical fluctuations the lattice of possible cuts were spaced widely enough to allow several MC events to fall between each placement. This does not, however, alleviate all concerns of a biased model. Some statistical fluctuation is still captured by optimization and un-checked this would lead to an under-prediction the standard model background because the selection is biased toward a low background content. To remove this bias, independent training and fitting data sets are used. All optimization was performed using the set of MC samples produced using Sherpa 2.2.1. The samples produced with Sherpa 2.2.10 provide a statistically independent and more statistically rich data set

which is used for validation and fitting. This means that the MC data used for fitting is isolated from the optimization of selection criteria.

Large negative weight removal.

Optimization Variables

Many analysis variables were explored for potential sensitivity, and those selected as having the best discrimination potential were tested in the final optimization. Presented below is a list of variables tested and their meaning.

- E_T^{miss} and \mathcal{S} : Missing transverse momentum and its significance.
- $p_T(\ell)$: Transverse momentum of signal lepton.
- $m_T(\ell, E_T^{miss})$: Transverse mass of lepton and E_T^{miss} system, given by

$$m_T(\ell, E_T^{miss}) = \sqrt{2p_{T,\ell}E_T^{miss} \left(1 - \cos(\phi_\ell - \phi_{E_T^{miss}})\right)} \quad (5.3)$$

- $m^{\text{TAR Jet}}$: Mass of the p_T -leading TAR jet calculated from the rescaled matched tracks.
- $p_T^{\text{TAR Jet}}$: Transverse momentum of the leading TAR jet.
- $D_2^{\beta=1}(\text{TAR Jet})$: Energy correlation function of the TAR jet, which helps to identify two-pronged jet substructure [33].
- **TAR Jet τ_{42}^{WTA} and τ_{21}^{WTA}** : N-Subjettiness ratios of the leading TAR jet, to identify two-pronged substructure [3].

In addition, a two-dimensional cut in the E_T^{miss} - $p_T(\ell)$ plane was considered during optimization.

Optimized Selection

The maximum mean expected significance across the four selected signal points was found to be achieved using the selection shown in Table 5.1.

In order to validate the choice of selection criteria “N-1” plots were produced which show the distribution of a variable with all but the cut on that variable applied. The expected asimov significance of placing a cut at each bin edge is then also calculated.

variable	requirement	reason
$N(\text{TAR Jets})$	> 0	W_{Cand} reconstruction
$m_T(\ell, E_T^{\text{miss}})$	$> 220 \text{ GeV}$	W+Jets Background Reduction
$m^{\text{TAR Jet}}$	$[68, 89] \text{ GeV}$	W_{Cand} reconstruction
\mathcal{S}	> 16	Select for high E_T^{miss}
$\Delta R(\text{TAR Jet}, \ell)$	< 1.2	Select for boosted $W_{\text{Cand}} + \ell\nu$ system
$D_2^{\beta=1}(\text{TAR Jet})$	< 1.1	2 Pronged W->qq Reco

Table 5.1: Optimized selection criteria for the “merged” category signal region.

These plots were produced using the W+Jets and Z+Jets samples produced in Sherpa 2.2.10 and are shown in Figure . They therefore demonstrates whether cuts are still placed at optimal or near-optimal locations using the final samples.

The plots validate the choice of cut placements, which are still at or near maximal significance.

5.4 Resolved Signal Region

Due to the highly boosted nature of most signal events, the hadronic W-decay products are most often able to be reconstructed as a TAR jet. As a result, the “resolved” signal region is considerably less sensitive than the “merged” signal region, but does provide an important enhancement especially at low s mass where the least boost is experienced. The “resolved” signal region selection criteria are listed in Table .

5.5 $t\bar{t}$ Control Regions

A control region is used to help constrain one or more sources of background in an analysis. It is designed as a region that covers a similar but orthogonal area of phase space to the signal region and is expected to contain many fewer signal events. As a result, the number of ATLAS data and MC simulated SM data events should in theory match very closely. Thus, a comparison ATLAS and MC data can be used in this region to help constrain the SM background predictions of MC in the signal region, ideally increasing accuracy and reducing uncertainty. $t\bar{t}$ is one of the three leading backgrounds in the both signal regions and this, along with a relatively simple path to a control region definition motivates creating one for each signal region.

Due to the fact that top quarks decay primarily to an W boson and b -quark, the principal cut excluding $t\bar{t}$ events from the signal regions is the veto of any events containing a b-tagged anti- k_t $R = 0.4$ jet. A natural path to defining a similar but orthogonal region rich in $t\bar{t}$ events would therefore be to simply reverse this cut and require at least 1 b-tagged jet. This scenario was found to be too signal rich, however, with only a reduction by factor of 10 and 4 in mean MC $\frac{\text{signal}}{\text{background}}$ from the “merged” and “resolved” signal regions.

To ameliorate this, the b-jet requirement was further pushed to 2 or more b-jets in the control region. This change sufficiently reduced signal contamination, but in the

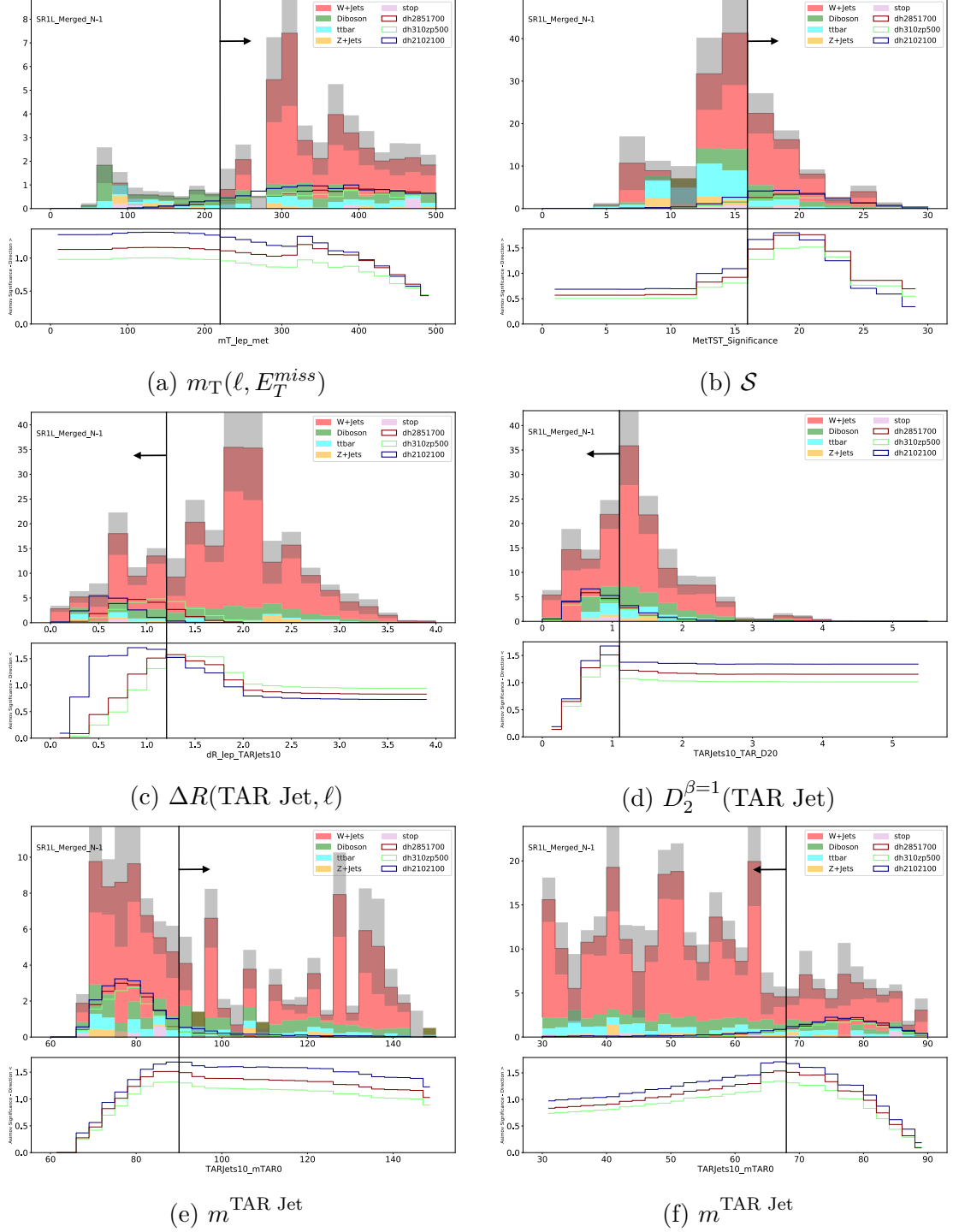


Figure 5.4: N-1 plots in the “merged” signal region.

“merged” control region it had the additional consequence of substantially reducing the number of events in the region, thereby reducing its statistical power. In response the \mathcal{S} cut was also loosened in the “merged” $t\bar{t}$ control region to $\mathcal{S} > 12$. Figure 5.5, which shows the number of weighted $t\bar{t}$ events expected in the “merged” control region for a given \mathcal{S} cut was used to motivate this choice.

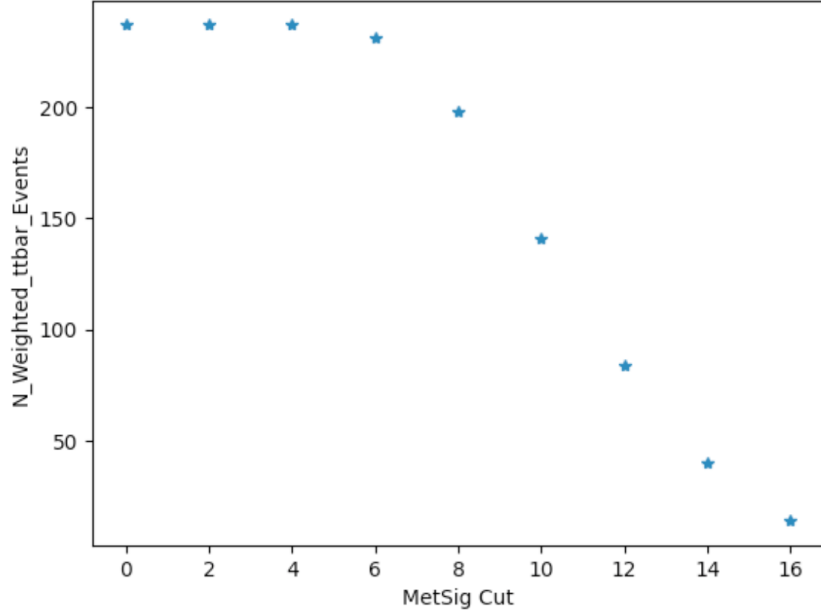


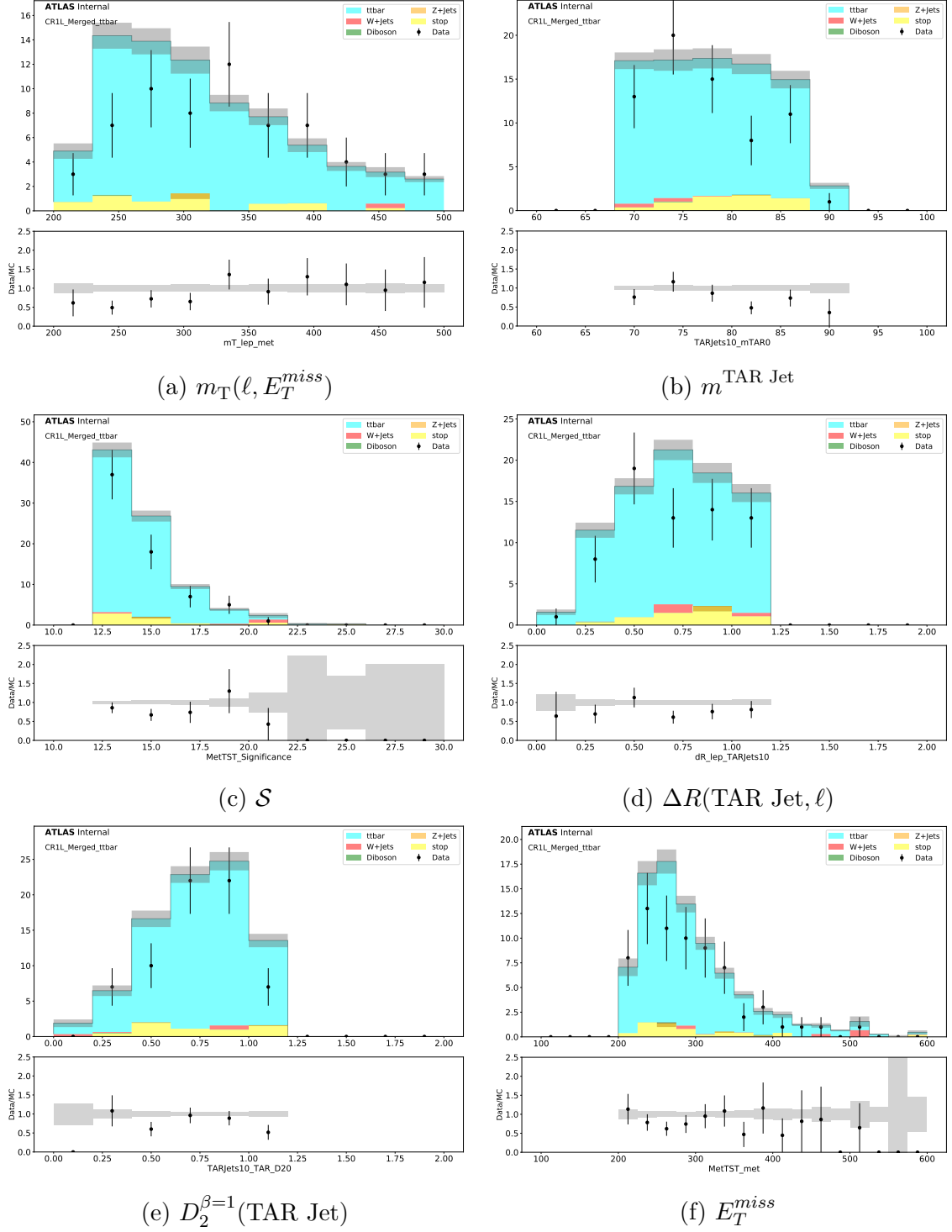
Figure 5.5: $t\bar{t}$ yield in the “merged” $t\bar{t}$ control region for various E_T^{miss} significance cut placements

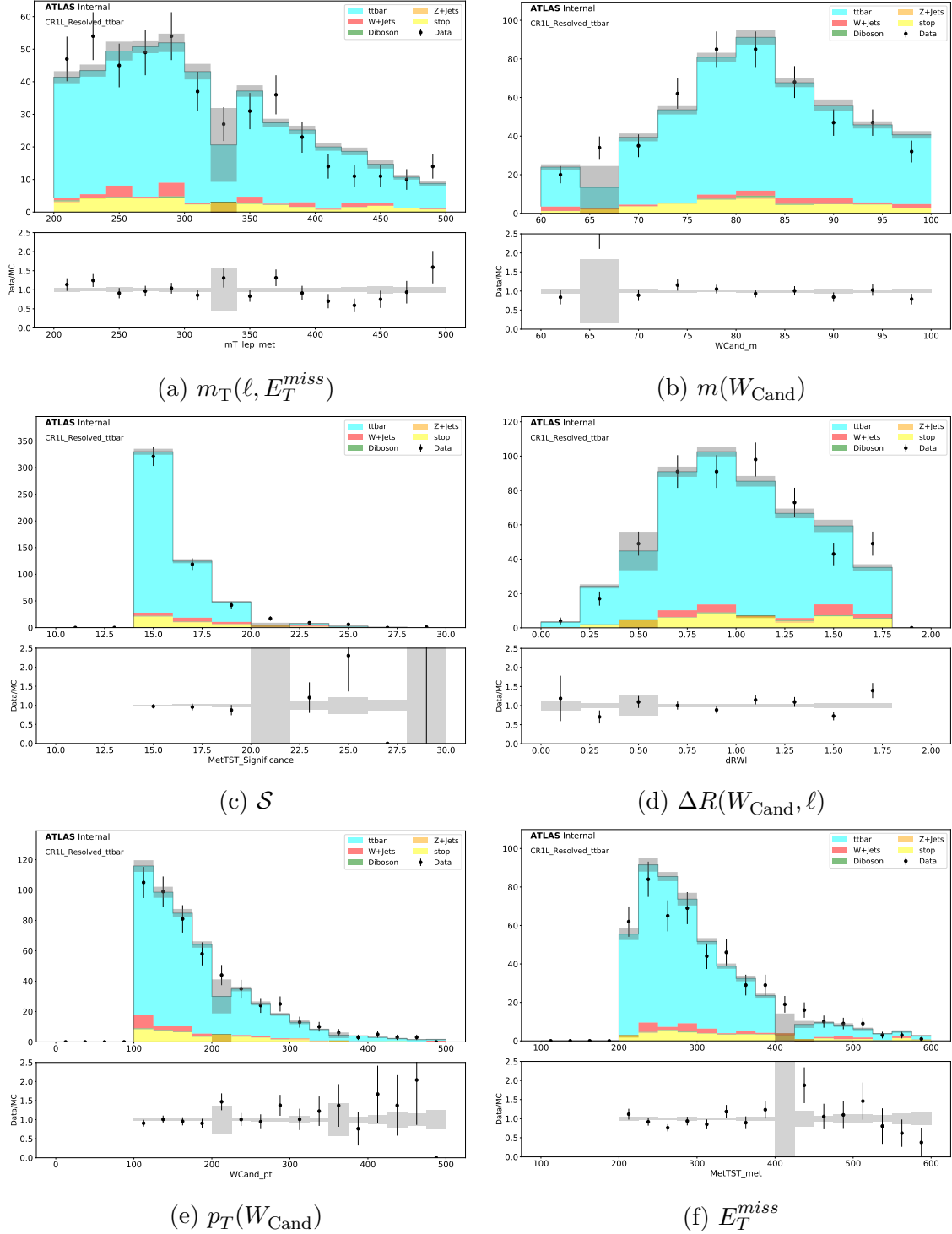
Table summarizes the differences in selection criteria between the “merged” and “resolved” signal and $t\bar{t}$ control regions.

Figures and show comparisons of the distributions of MC and ATLAS data in the $t\bar{t}$ control regions. These demonstrate a slight over-prediction of yield from MC in the “merged” region, which will be used to constrain the $t\bar{t}$ background in the signal region. The difference between data and MC distributions does not show a strong correlation with any of the analysis variables.

5.6 $W+jets$ Control Region

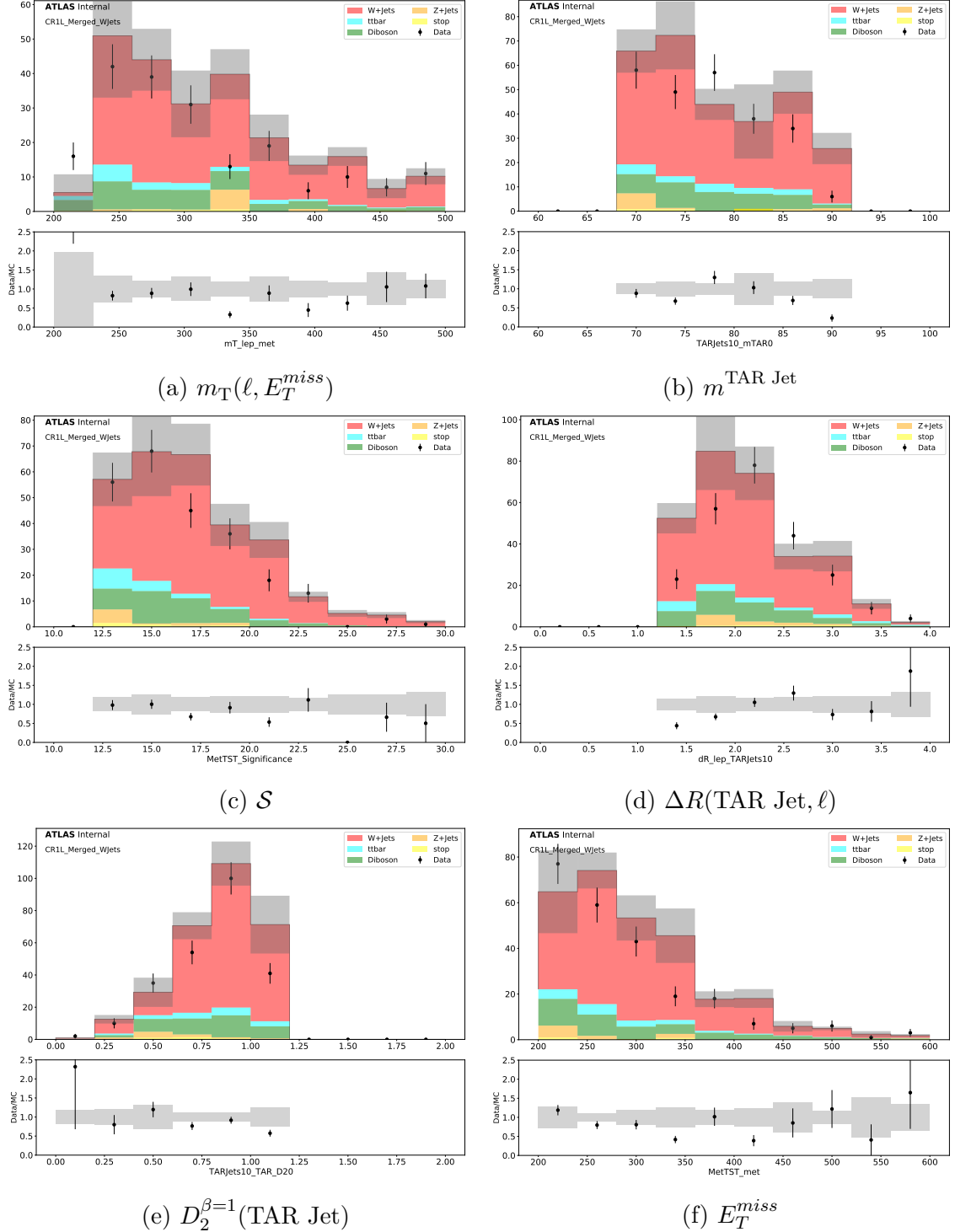
An additional pair of control regions are defined in order to constrain the dominant $W+jets$ background in the signal regions. These regions are defined by reversing the

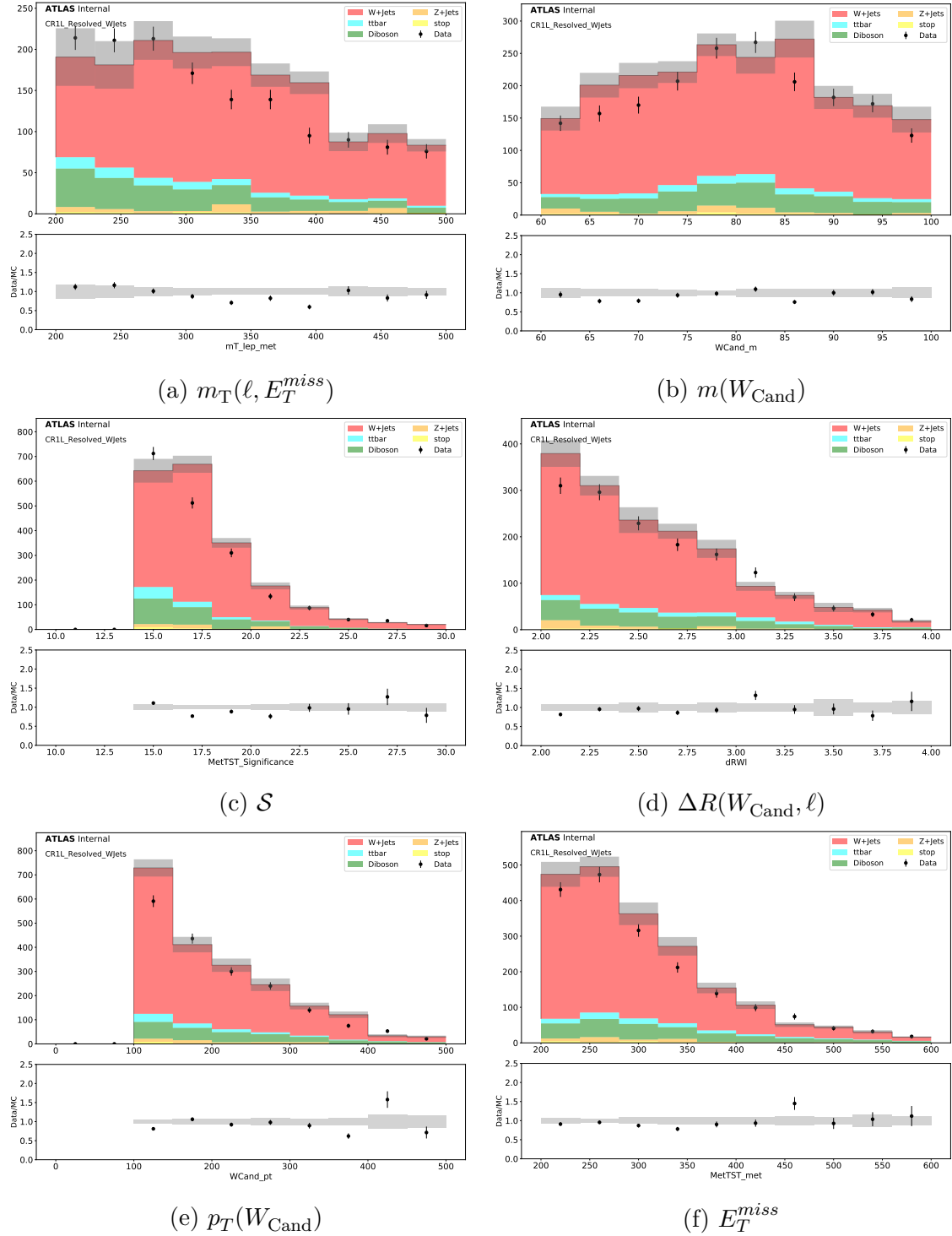
Figure 5.6: Data-MC Comparisons in the “merged” $t\bar{t}$ control region

Figure 5.7: Data-MC Comparisons in the “resolved” $t\bar{t}$ control region

$\Delta R(\text{TAR Jet}, \ell)$ and $\Delta R(W_{\text{Cand}}, \ell)$ cuts in the “merged” and “resolved” signal regions. This reverses the position of the neutrino and charged lepton in the W decay without substantially altering the remaining kinematics of the event that allow the hadronic activity to fake a second W . In the “merged” $W + \text{jets}$ control region the \mathcal{S} cut is reduced to $\mathcal{S} > 12$ in order to improve statistical power.

Table summarizes the differences in selection criteria between the “merged” and “resolved” signal and $W + \text{jets}$ control regions.

Figure 5.8: Data-MC comparisons in the “merged” $W+jets$ control region

Figure 5.9: Data-MC comparisons in the “resolved” $W + \text{jets}$ control region

Chapter 6

Conclusions

My first rule for this chapter is to avoid finishing it with a section talking about future work. It may seem logical, yet it also appears to give a list of all items which remain undone! It is not the best way psychologically.

This chapter should contain a mirror of the introduction, where a summary of the *extraordinary* new results and their wonderful attributes should be stated first, followed by an executive summary of how this new solution was arrived at. Consider the practical fact that this chapter will be read quickly at the beginning of a review (thus it needs to provide a strong impact) and then again in depth at the very end, perhaps a few days after the details of the previous 3 chapters have been somehow forgotten. Reinforcement of the positive is the key strategy here, without of course blowing hot air.

One other consideration is that some people like to join the chapter containing the analysis with the only with conclusions. This can indeed work very well in certain topics.

Finally, the conclusions do not appear only in this chapter. This sample mini thesis lacks a feature which I regard as absolutely necessary, namely a short paragraph at the end of each chapter giving a brief summary of what was presented together with a one sentence preview as to what might expect the connection to be with the next chapter(s). You are writing a story, the *story of your wonderful research work*. A story needs a line connecting all its parts and you are responsible for these linkages.

Appendix A

Additional Information

A.1 Preselection level plots

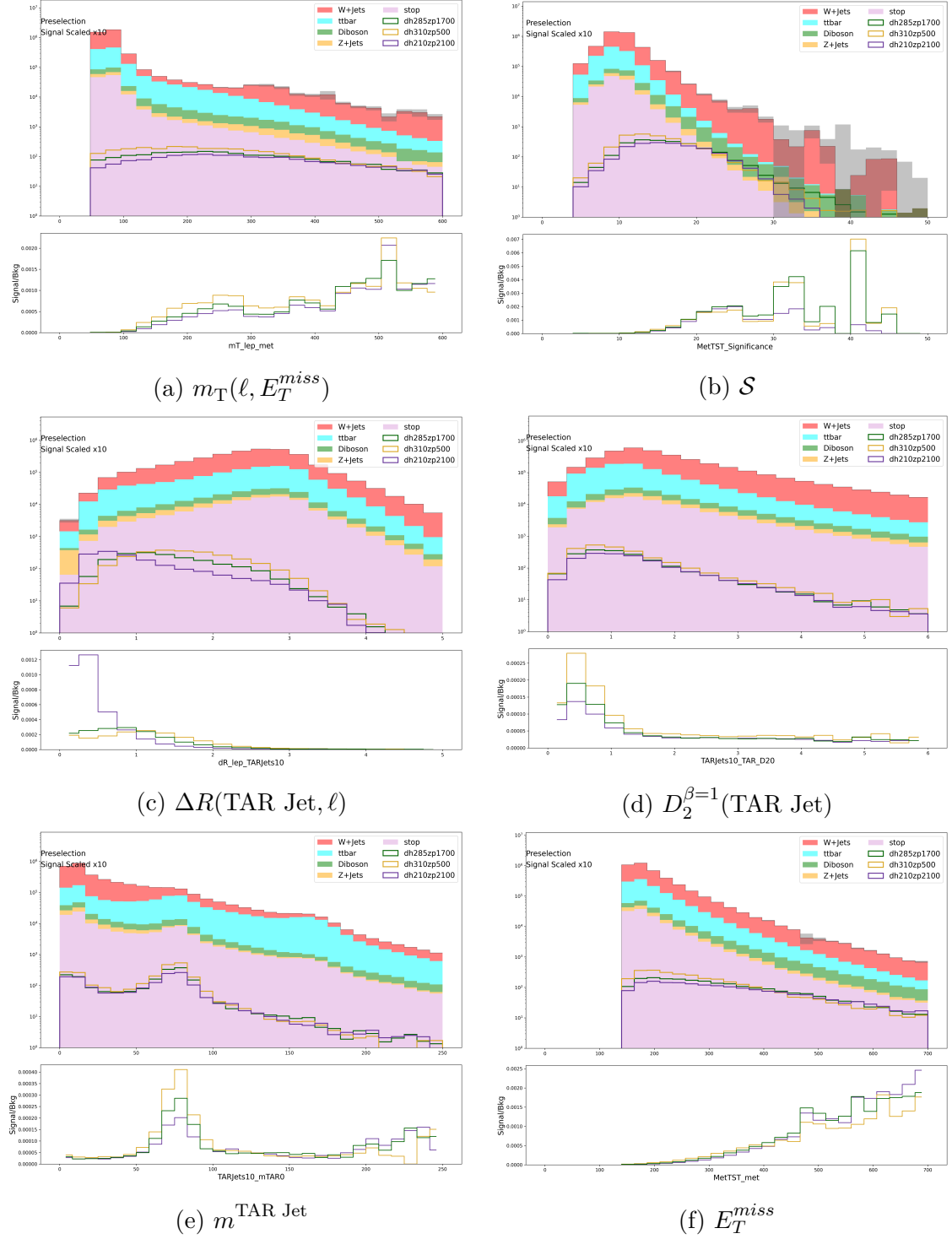


Figure A.1: N-1 plots in the “merged” signal region.

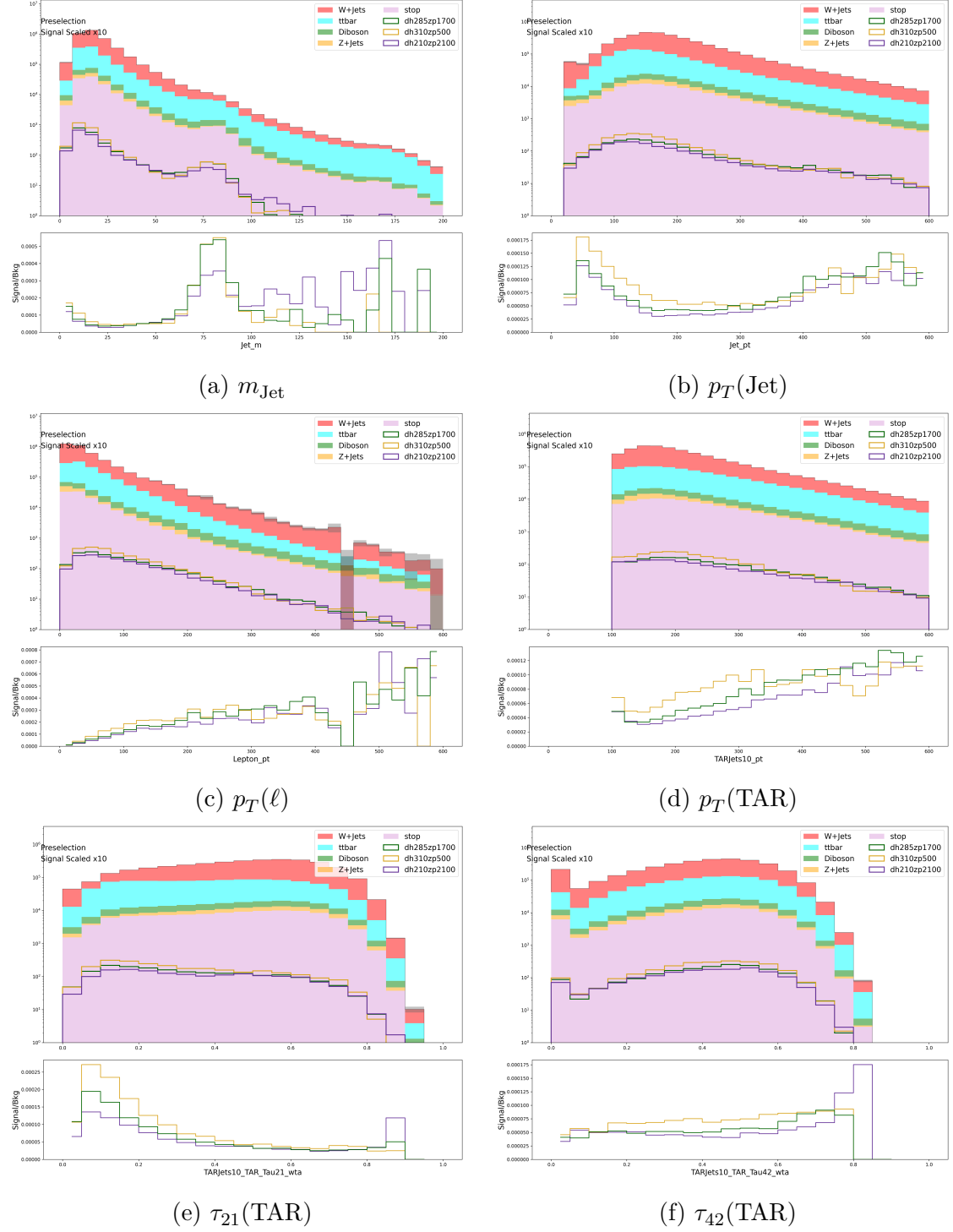


Figure A.2: N-1 plots in the “merged” signal region.

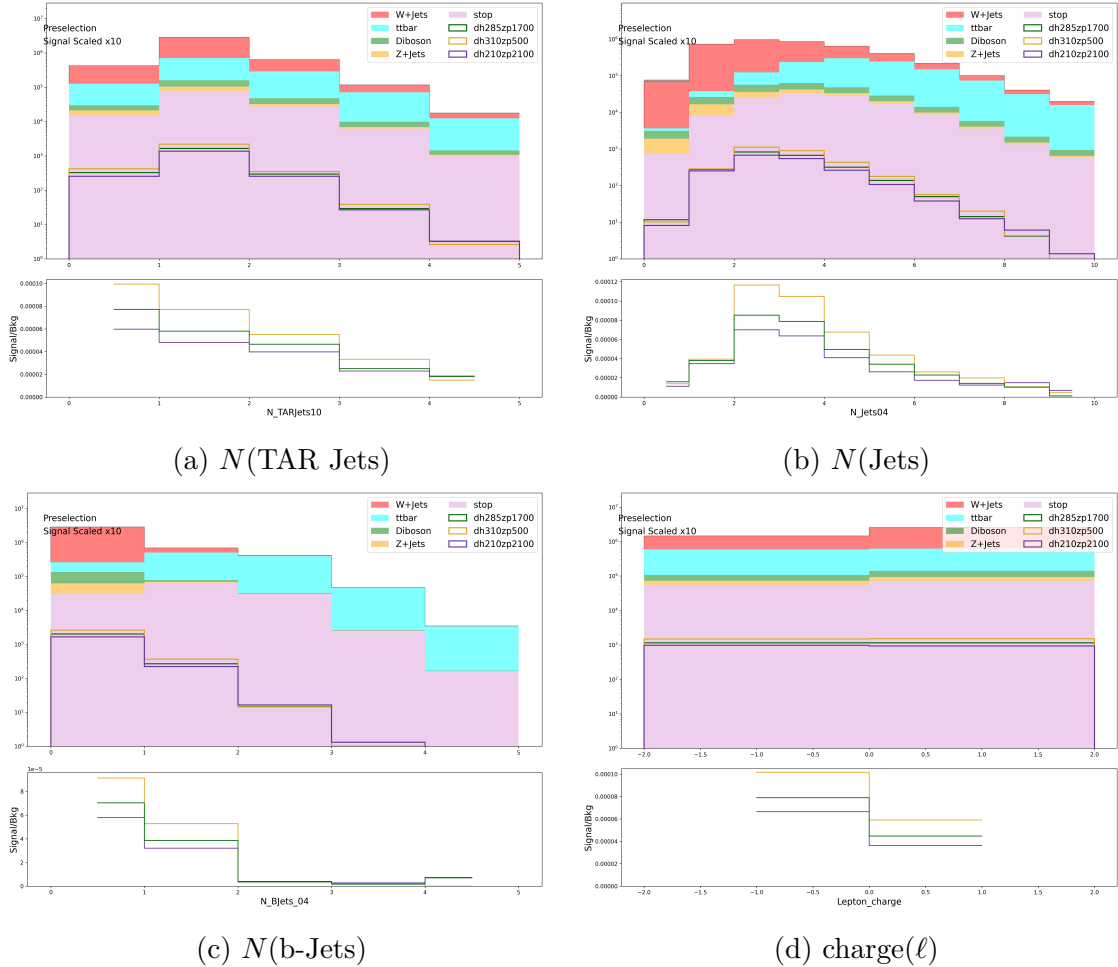


Figure A.3: N-1 plots in the “merged” signal region.

Bibliography

- [1] Morad Aaboud et al. “Electron reconstruction and identification in the ATLAS experiment using the 2015 and 2016 LHC proton-proton collision data at $\sqrt{s} = 13$ TeV”. In: *Eur. Phys. J. C* 79.8 (2019), p. 639. DOI: 10.1140/epjc/s10052-019-7140-6. arXiv: 1902.04655 [physics.ins-det].
- [2] Morad Aaboud et al. “Jet reconstruction and performance using particle flow with the ATLAS Detector”. In: *Eur. Phys. J. C* 77.7 (2017), p. 466. DOI: 10.1140/epjc/s10052-017-5031-2. arXiv: 1703.10485 [hep-ex].
- [3] Morad Aaboud et al. “Measurement of jet-substructure observables in top quark, W boson and light jet production in proton-proton collisions at $\sqrt{s} = 13$ TeV with the ATLAS detector”. In: *JHEP* 08 (2019), p. 033. DOI: 10.1007/JHEP08(2019)033. arXiv: 1903.02942 [hep-ex].
- [4] G. Aad et al. “Observation of a new particle in the search for the Standard Model Higgs boson with the ATLAS detector at the LHC”. In: *Physics Letters B* 716.1 (2012), pp. 1–29. ISSN: 0370-2693. DOI: <https://doi.org/10.1016/j.physletb.2012.08.020>.
- [5] G Aad et al. “The ATLAS Experiment at the CERN Large Hadron Collider”. In: *JINST* 3 (2008). Also published by CERN Geneva in 2010, S08003. 437 p. DOI: 10.1088/1748-0221/3/08/S08003. URL: <https://cds.cern.ch/record/1129811>.
- [6] Georges Aad et al. “Muon reconstruction performance of the ATLAS detector in proton–proton collision data at $\sqrt{s} = 13$ TeV”. In: *Eur. Phys. J. C* 76.5 (2016), p. 292. DOI: 10.1140/epjc/s10052-016-4120-y. arXiv: 1603.05598 [hep-ex].
- [7] Georges Aad et al. “Search for Dark Matter Produced in Association with a Dark Higgs Boson Decaying into $W^\pm W^\mp$ or ZZ in Fully Hadronic Final States

- from $\sqrt{s} = 13$ TeV pp Collisions Recorded with the ATLAS Detector”. In: *Phys. Rev. Lett.* 126.12 (2021), p. 121802. DOI: 10.1103/PhysRevLett.126.121802. arXiv: 2010.06548 [hep-ex].
- [8] Georges Aad et al. “Topological cell clustering in the ATLAS calorimeters and its performance in LHC Run 1”. In: *Eur. Phys. J. C* 77 (2017), p. 490. DOI: 10.1140/epjc/s10052-017-5004-5. arXiv: 1603.02934 [hep-ex].
 - [9] Simone Alioli et al. “A general framework for implementing NLO calculations in shower Monte Carlo programs: the POWHEG BOX”. In: *JHEP* 06 (2010), p. 043. DOI: 10.1007/JHEP06(2010)043. arXiv: 1002.2581 [hep-ph].
 - [10] J. Alwall et al. “The automated computation of tree-level and next-to-leading order differential cross sections, and their matching to parton shower simulations”. In: *JHEP* 07 (2014), p. 079. DOI: 10.1007/JHEP07(2014)079. arXiv: 1405.0301 [hep-ph].
 - [11] *ATLAS simulation of boson plus jets processes in Run 2*. Tech. rep. All figures including auxiliary figures are available at <https://atlas.web.cern.ch/Atlas/GROUPS/PHYSICS/PUBNOTES/ATL-PHYS-PUB-2017-006>. Geneva: CERN, 2017. URL: <https://cds.cern.ch/record/2261937>.
 - [12] Richard D. Ball et al. “Parton distributions for the LHC Run II”. In: *JHEP* 04 (2015), p. 040. DOI: 10.1007/JHEP04(2015)040. arXiv: 1410.8849 [hep-ph].
 - [13] Richard D. Ball et al. “Parton distributions with LHC data”. In: *Nucl. Phys. B* 867 (2013), pp. 244–289. DOI: 10.1016/j.nuclphysb.2012.10.003. arXiv: 1207.1303 [hep-ph].
 - [14] Enrico Bothmann et al. “Event Generation with Sherpa 2.2”. In: *SciPost Phys.* 7.3 (2019), p. 034. DOI: 10.21468/SciPostPhys.7.3.034. arXiv: 1905.09127 [hep-ph].
 - [15] Matteo Cacciari, Gavin P. Salam, and Gregory Soyez. “The anti- k_t jet clustering algorithm”. In: *JHEP* 04 (2008), p. 063. DOI: 10.1088/1126-6708/2008/04/063. arXiv: 0802.1189 [hep-ph].
 - [16] John Campbell, Joey Huston, and Frank Krauss. *The black book of quantum chromodynamics: a primer for the LHC era*. Oxford: Oxford University Press, 2018. DOI: 10.1093/oso/9780199652747.001.0001.

- [17] Douglas Clowe et al. “A direct empirical proof of the existence of dark matter”. In: *Astrophys. J. Lett.* 648 (2006), pp. L109–L113. DOI: 10.1086/508162. arXiv: astro-ph/0608407.
- [18] Glen Cowan et al. “Asymptotic formulae for likelihood-based tests of new physics”. In: *Eur. Phys. J. C* 71 (2011). [Erratum: Eur.Phys.J.C 73, 2501 (2013)], p. 1554. DOI: 10.1140/epjc/s10052-011-1554-0. arXiv: 1007.1727 [physics.data-an].
- [19] S. Dittmaier et al. “Handbook of LHC Higgs Cross Sections: 1. Inclusive Observables”. In: (Jan. 2011). DOI: 10.5170/CERN-2011-002. arXiv: 1101.0593 [hep-ph].
- [20] Michael Duerr et al. “Hunting the dark Higgs”. In: *JHEP* 04 (2017), p. 143. DOI: 10.1007/JHEP04(2017)143. arXiv: 1701.08780 [hep-ph].
- [21] F Englert and R Brout. “Broken symmetry and the masses of gauge vector mesons”. In: *Phys. Rev. Lett.* 13 (1964), pp. 321–323. DOI: 10.1103/PhysRevLett.13.321.
- [22] “LHC Machine”. In: *JINST* 3 (2008). Ed. by Lyndon Evans and Philip Bryant, S08001. DOI: 10.1088/1748-0221/3/08/S08001.
- [23] Richard P Feynman. *QED: The Strange Theory of Light and Matter*. Princeton, NJ: Princeton University Press, 2008. ISBN: 9780691164090.
- [24] Matthew Gignac et al. *Single Vector-Boson Monte Carlo setups for ATLAS Run 2 physics*. Tech. rep. Geneva: CERN, 2021. URL: <https://cds.cern.ch/record/2753199>.
- [25] Sheldon L. Glashow. “Partial-symmetries of weak interactions”. In: *Nuclear Physics* 22.4 (1961), pp. 579–588. ISSN: 0029-5582. DOI: [https://doi.org/10.1016/0029-5582\(61\)90469-2](https://doi.org/10.1016/0029-5582(61)90469-2).
- [26] Jeffrey Goldstone, Abdus Salam, and Steven Weinberg. “Broken Symmetries”. In: *Phys. Rev.* 127 (3 1962), pp. 965–970. DOI: 10.1103/PhysRev.127.965.
- [27] David J Griffiths. *Introduction to elementary particles; 2nd rev. version*. New York, NY: Wiley, 2008.
- [28] Particle Data Group et al. “Review of Particle Physics”. In: *Progress of Theoretical and Experimental Physics* 2020.8 (Aug. 2020). ISSN: 2050-3911.

- [29] Peter W. Higgs. “Broken Symmetries and the Masses of Gauge Bosons”. In: *Phys. Rev. Lett.* 13 (1964). Ed. by J. C. Taylor, pp. 508–509. DOI: 10.1103/PhysRevLett.13.508.
- [30] Peter W. Higgs. “Spontaneous Symmetry Breakdown without Massless Bosons”. In: *Phys. Rev.* 145 (1966), pp. 1156–1163. DOI: 10.1103/PhysRev.145.1156.
- [31] Stefan Hoeche et al. “QCD matrix elements + parton showers: The NLO case”. In: *JHEP* 04 (2013), p. 027. DOI: 10.1007/JHEP04(2013)027. arXiv: 1207.5030 [hep-ph].
- [32] *Identification of Jets Containing b-Hadrons with Recurrent Neural Networks at the ATLAS Experiment*. Tech. rep. All figures including auxiliary figures are available at <https://atlas.web.cern.ch/Atlas/GROUPS/PHYSICS/PUBNOTES/ATL-PHYS-PUB-2017-003>. Geneva: CERN, 2017. URL: <https://cds.cern.ch/record/2255226>.
- [33] Andrew J. Larkoski, Gavin P. Salam, and Jesse Thaler. “Energy Correlation Functions for Jet Substructure”. In: *JHEP* 06 (2013), p. 108. DOI: 10.1007/JHEP06(2013)108. arXiv: 1305.0007 [hep-ph].
- [34] Leif Lonnblad and Stefan Prestel. “Matching Tree-Level Matrix Elements with Interleaved Showers”. In: *JHEP* 03 (2012), p. 019. DOI: 10.1007/JHEP03(2012)019. arXiv: 1109.4829 [hep-ph].
- [35] *Object-based missing transverse momentum significance in the ATLAS detector*. Tech. rep. All figures including auxiliary figures are available at <https://atlas.web.cern.ch/Atlas/GROUPS/PHYSICS/CONFNOTES/ATLAS-CONF-2018-038>. Geneva: CERN, 2018. URL: <https://cds.cern.ch/record/2630948>.
- [36] M.E. Peskin and D.V. Schroeder. *An Introduction To Quantum Field Theory*. Frontiers in Physics. Avalon Publishing, 1995. ISBN: 9780813345437.
- [37] *RECAST framework reinterpretation of an ATLAS Dark Matter Search constraining a model of a dark Higgs boson decaying to two b-quarks*. Tech. rep. All figures including auxiliary figures are available at <https://atlas.web.cern.ch/Atlas/GROUPS/PHYSICS/PUBNOTES/ATL-PHYS-PUB-2019-032>. Geneva: CERN, 2019. URL: <http://cds.cern.ch/record/2686290>.

- [38] V. C. Rubin, Jr. Ford W. K., and N. Thonnard. “Rotational properties of 21 SC galaxies with a large range of luminosities and radii, from NGC 4605 ($R=4\text{kpc}$) to UGC 2885 ($R=122\text{kpc}$).” In: *Astrophysical Journal* 238 (June 1980), pp. 471–487. DOI: [10.1086/158003](https://doi.org/10.1086/158003).
- [39] M.D. Schwartz. *Quantum Field Theory and the Standard Model*. Cambridge University Press, 2014. ISBN: 9781107034730.
- [40] Torbjörn Sjöstrand et al. “An introduction to PYTHIA 8.2”. In: *Comput. Phys. Commun.* 191 (2015), pp. 159–177. DOI: [10.1016/j.cpc.2015.01.024](https://doi.org/10.1016/j.cpc.2015.01.024). arXiv: [1410.3012 \[hep-ph\]](https://arxiv.org/abs/1410.3012).
- [41] *Tagging and suppression of pileup jets with the ATLAS detector*. Tech. rep. All figures including auxiliary figures are available at <https://atlas.web.cern.ch/Atlas/GROUPS/PHYSICS/CONFNOTES/ATLAS-CONF-2014-018>. Geneva: CERN, 2014. URL: <https://cds.cern.ch/record/1700870>.
- [42] *Track assisted techniques for jet substructure*. Tech. rep. All figures including auxiliary figures are available at <https://atlas.web.cern.ch/Atlas/GROUPS/PHYSICS/PUB-NOTES/ATL-PHYS-PUB-2018-012>. Geneva: CERN, 2018. URL: <https://cds.cern.ch/record/2630864>.
- [43] Steven Weinberg. “A Model of Leptons”. In: *Phys. Rev. Lett.* 19 (21 1967), pp. 1264–1266. DOI: [10.1103/PhysRevLett.19.1264](https://doi.org/10.1103/PhysRevLett.19.1264).
- [44] F. Zwicky. “On the Masses of Nebulae and of Clusters of Nebulae”. In: *Astrophysical Journal* 86 (Oct. 1937), p. 217. DOI: [10.1086/143864](https://doi.org/10.1086/143864).